

RESEARCH ARTICLE

10.1002/2014JC009931

Observed wintertime tidal and subtidal currents over the continental shelf in the northern South China Sea

Special Section:

Pacific-Asian Marginal Seas

Ruixiang Li¹, Changsheng Chen^{2,3}, Huayong Xia¹, Robert C. Beardsley⁴, Maochong Shi⁵, Zhigang Lai⁶, Huichan Lin², Yanqing Feng¹, Changjian Liu¹, Qichun Xu², Yang Ding⁵, and Yu Zhang²

Key Points:

- Observed diurnal tides were characterized by first mode baroclinic Kelvin waves
- The wind-induced southwestward flows and eddies prevailed during the winter
- Observations did not support the existence of the South China Sea Warm Current

Correspondence to:

R. Li,
liruixian05@mails.gucas.ac.cn

Citation:

Li, R., et al. (2014), Observed wintertime tidal and subtidal currents over the continental shelf in the northern South China Sea, *J. Geophys. Res. Oceans*, 119, doi:10.1002/2014JC009931.

Received 25 FEB 2014

Accepted 31 JUL 2014

Accepted article online 4 AUG 2014

¹South China Sea Marine Engineering Survey Center, State Ocean Administration, Guangzhou, People's Republic of China, ²School for Marine Science and Technology, University of Massachusetts-Dartmouth, New Bedford, Massachusetts, USA, ³International Center for Marine Studies, Shanghai Ocean University, Shanghai, People's Republic of China, ⁴Department of Physical Oceanography, Woods Hole Oceanographic Institution, Woods Hole, Massachusetts, USA, ⁵College of Physical and Environmental Oceanography, Ocean University of China, Qingdao, People's Republic of China, ⁶School of Marine Sciences, Sun Yat-Sen University, Guangzhou, People's Republic of China

Abstract Synthesis analyses were performed to examine characteristics of tidal and subtidal currents at eight mooring sites deployed over the northern South China Sea (NSCS) continental shelf in the 2006–2007 and 2009–2010 winters. Rotary spectra and harmonic analysis results showed that observed tidal currents in the NSCS were dominated by baroclinic diurnal tides with phases varying both vertically and horizontally. This feature was supported by the CC-FVCOM results, which demonstrated that the diurnal tidal flow over this shelf was characterized by baroclinic Kelvin waves with vertical phase differences varying in different flow zones. The northeasterly wind-induced southwestward flow prevailed over the NSCS shelf during winter, with episodic appearances of mesoscale eddies and a bottom-intensified buoyancy-driven slope water intrusion. The moored current records captured a warm-core anticyclonic eddy, which originated from the southwestern coast of Taiwan and propagated southwestward along the slope consistent with a combination of β -plane and topographic Rossby waves. The eddy was surface-intensified with a swirl speed of >50 cm/s and a vertical scale of ~ 400 m. In absence of eddies and onshore deep slope water intrusion, the observed southwestward flow was highly coherent with the northeasterly wind stress. Observations did not support the existence of the permanent wintertime South China Sea Warm Current (SCSWC). The definition of SCSWC, which was based mainly on thermal wind calculations with assumed level of no motion at the bottom, needs to be interpreted with caution since the observed circulation over the NSCS shelf in winter included both barotropic and baroclinic components.

1. Introduction

The South China Sea (SCS), the largest marginal Sea in the western Pacific Ocean, features a broad shallow shelf, narrow steep slope, and deep basin. The northern SCS (hereafter referred to as NSCS) is defined as the region bounded by Hainan Island on the south and Taiwan on the north in the range of 106°E – 121°E in longitude and 17°N – 24°N in latitude (Figure 1). This region contains a broad continental shelf connecting to the Pacific Ocean through Luzon Strait and to the East China Sea through Taiwan Strait. The shelf bathymetry gradually changes from a few meters near the coast to ~ 200 m over a shelf width of 200–300 km and then deepens rapidly to 1000 m over the shelfbreak within a distance of a few to 10 km. The slope of the NSCS shelf increases from the south to north in a range of ~ 0.018 to ~ 0.03 .

Flow over the NSCS continental shelf is driven by tides, surface meteorological forcing (seasonal monsoon, heat flux, and evaporation minus precipitation), and lateral boundary water fluxes from rivers and westward intrusion of the Kuroshio through Luzon Strait. The tidal energy over this shelf is mainly from tidal waves propagating through Luzon Strait from the western Pacific Ocean and through Taiwan Strait from the East China Sea [Fang et al., 1999; Zu et al., 2008; Beardsley et al., 2004]. Of most importance are energetic internal tides, which originate from Luzon Strait as barotropic tidal waves climb over submerged ridges [Lien et al., 2005; Jan et al., 2007] and intensify over the shelfbreak as a result of interaction of surface tidal currents with steep bottom topography in stratified conditions [Zhao et al., 2004; Chang et al., 2006]. Both barotropic and internal tides in this region are dominated by four major tidal constituents: K_1 (25.83 h) and O_1

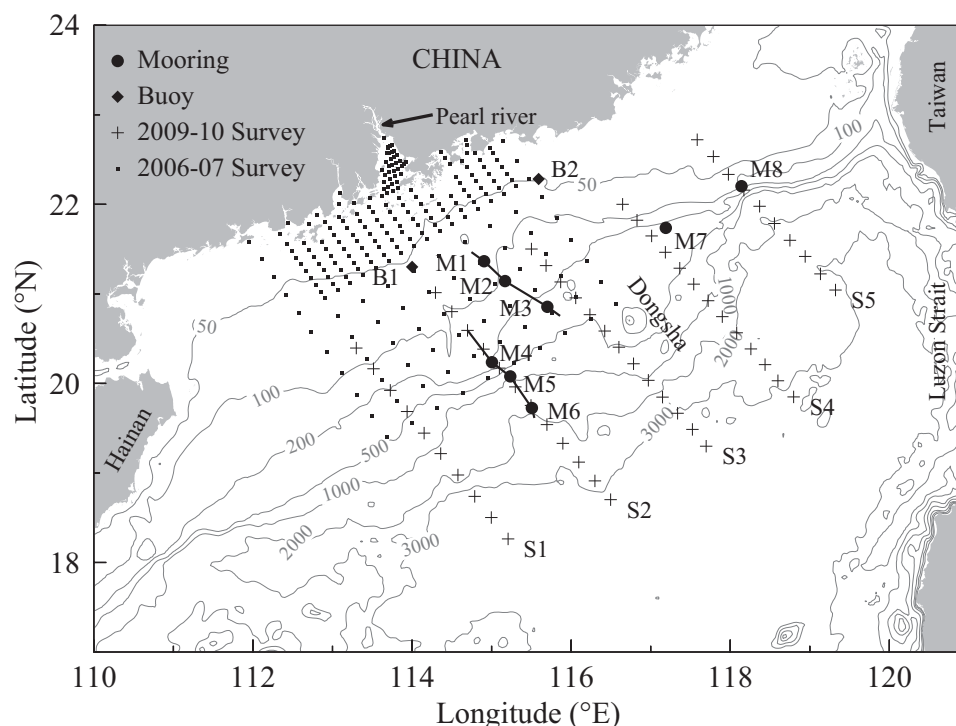


Figure 1. Maps of bathymetry and locations of moorings M1–M8, buoys B1–B2, and hydrographic survey sites conducted in winter seasons of 2006–2007 and 2009–2010 over the NSCS shelf. Labels S1–S5 indicate the cross-shelf CTD transects. Transects of M1–M3 and M4–M6 are defined as lines connected these sites shown in figure.

(23.94 h) at diurnal periods and M_2 (12.42 h) and S_2 (12.00 h) at semidiurnal periods [Fang *et al.*, 1999; Duda *et al.*, 2004]. The internal tides are stronger at diurnal periods than at semidiurnal periods, enhanced in summer and weakened in winter [Liang *et al.*, 2005; Guo *et al.*, 2006, 2012; Klymak *et al.*, 2011]. Previous studies show that the diurnal internal tidal flow can be considered as the first baroclinic mode in the vertical, while the semidiurnal internal tidal flow decreases monotonically as the water becomes deep [Duda and Rainville, 2008; Xu *et al.*, 2013]. Since most past current measurements have been made locally or restricted on a single cross-isobath transect, no measurements have been made to examine the spatial structure of the internal tidal flow over the NSCS shelf due to the lack of an array of time series measurements with spatial coverage similar or larger than the wavelength of the internal tidal waves.

The SCS is in the East Asian monsoon climate system, with northeasterly wind (blowing from the northeast direction) prevailing in winter and southwesterly wind in summer. The monsoon-driven basin-scale circulation is cyclonic in winter and anticyclonic in summer [Wyrski, 1961; Xu *et al.*, 1982; Ding *et al.*, 2013]. As a portion of this seasonal wind-driven circulation system, the near-surface flow over the NSCS continental shelf is southwestward in winter and northeastward in summer. Near the coastal region, during the downwelling-favorable northeasterly winter monsoon, the wind produces an onshore Ekman transport, intensifying the southwestward buoyancy-driven flow that forms as a result of freshwater discharge from the Pearl River. This wind and buoyancy-driven current flows southwestward parallel to the local coastline and is named the Guangdong Coastal Current [Fang *et al.*, 1998]. Importance of wind forcing to the variability of the near-shore coastal currents has been verified in many previous observational and modeling studies [e.g., Kourafalou *et al.*, 1996; Chen and Xie, 1997; Chen, 2000]. Due to the lack of direct current measurements over the mid and outer NSCS shelf, however, it is unclear whether or not the wind-driven circulation is also a dominant feature in this region during the winter season.

Guan and Chen [1964] and Guan [1978] first suggested that there is a counter-wind current originating in the vicinity of Hainan Island and flowing northeastward between the 200 and 400 m isobaths over the mid-shelf during winter. Based primarily on analysis of hydrographic data through the geostrophic calculation relative to a reference level of no motion at the bottom, they named this current the South China Sea Warm Current (SCSWC), with a length of about 160–300 km and a maximum surface velocity of >30 cm/s.

Although this current was produced in some previous model results under idealized or climatological forcing conditions [Hsueh and Zhong, 2004; Xue et al., 2004; Yang et al., 2008], it is unclear whether or not this current is a permanent wintertime feature over the NSCS continental shelf.

Mesoscale eddies are active and energetic in the NSCS, with frequent appearances on the southwest coast of Taiwan and in the northwest area of Luzon Strait [Wang et al., 2003]. Kinematic and dynamic features of these eddies are complex: some occurred, intensified, and dissipated locally, and others moved southwestward along the slope and became re-intensified when they arrived over the southeastern shelf of Hainan Island [Yuan et al., 2007]. Since the diameters of these eddies were >100 km [Liu et al., 2012], they were easily detected and verified from satellite-derived sea surface height data. They typically moved at a speed of ~ 10 cm/s, which was similar to the phase speed of westward propagating Rossby waves in the NSCS [Wang et al., 2008]. These eddies were also captured in temperature and salinity profiles from previous hydrographic surveys, which showed that the vertical scale of these eddies was about 1000 m over the slope [Li et al., 1998; Liu et al., 2012]. Due to the lack of direct current measurements, however, the horizontal and vertical structure of the flow field within these eddies is not well explored yet. Is the flow field observed within these eddies in geostrophic balance? Could eddy currents intensify near the bottom when they are near the shelfbreak? Do these eddies influence the regional circulation over the NSCS continental shelf? These questions are best addressed with direct current measurements.

Flow over the NSCS slope is influenced by the Kuroshio intrusion through Luzon Strait [Su et al., 1990; Shaw, 1991; Farris and Wimbush, 1996; Metzger and Hurlburt, 2001; Caruso et al., 2006; Matsuno et al., 2009; Tai et al., 2010]. Past studies have revealed two major features: (a) the Kuroshio intrusion into the SCS occurred most frequently during late fall, winter, and spring when strong NE monsoon winds prevailed, and (b) the region influenced directly by the Kuroshio intrusion was restricted mainly to the NSCS west of Luzon Strait and around Taiwan. The intrusion could be initiated or driven under NE monsoon winds [Farris and Wimbush, 1996], changes of the Kuroshio transport [Shaw, 1991], and baroclinic instability [Tai et al., 2010]. Caruso et al. [2006] examined the interannual variability of Kuroshio intrusion events into the SCS, and their results suggested that the path of the intruded water within the NSCS could be much more complex than a simple loop current. A relatively strong, southwestward along-isobath flow was often observed at the shelfbreak of the NSCS, which was believed as a branch of the Kuroshio intrusion water [Guo et al., 1985] or could form as a result of an intensified western boundary current of the cyclonic gyre in the SCS [Su, 2004]. While current measurements have been made across Luzon Strait to monitor and assess the Kuroshio intrusion process into the SCS, few direct current measurements were made over the NSCS continental shelf to capture intrusion events. Could the intruded Kuroshio water penetrate onto the midshelf of the NSCS? If so, how could it influence the circulation there? To our knowledge, these questions have not well addressed in previous studies.

This paper attempts to address some of the questions raised above by synthesis of current data collected on eight moorings deployed in the winters of 2006–2007 and 2009–2010. The remaining sections are organized as follow. Section 2 describes the data set and model used in this study. Section 3 presents the observed spatial distribution of barotropic and internal tidal currents, followed by a discussion with barotropic and baroclinic tidal model simulations. Section 4 first depicts the observed temporal variability and spatial distribution of low-passed subtidal currents and then discusses the wind-driven mechanism for the wintertime circulation over the NSCS shelf. Finally, section 5 summarizes the conclusion.

2. The Data and Model

2.1. Field Measurements

Eight moored ADCPs (named M1–M8) were deployed over the NSCS continental shelf in the winters of 2006–2007 and 2009–2010 (Figure 1 and Table 1), covering a region of ~ 300 km in the along-isobath direction and ~ 160 km in the cross-isobath direction with a depth range from 90 to 2000 m. M1, M2, and M3 were deployed on a cross-shelf line in the midshelf with a water depth range of 90–280 m, while M4, M5, and M6 were located on a cross-shelfbreak line where the water depth changed rapidly from 200 to 800 m over a distance of 30 km and then gradually deepened to 2000 m over a distance of 48 km. M7 and M8 were placed around the 200 m isobath on the northeast of Dongsha Island. M1–M4 and M7–M8 were equipped with bottom-mounted, upward looking ADCPs, while upward looking ADCPs on M5 and M6 were

Table 1. Location, DEPTH, Time, Record Length, Instrument, Sample Depth, and Sampling Interval of Moorings Deployed in the NSCS in Winter 2006 and 2009

Station	Depth (m)	Longitude (E)	Latitude (N)	Date Range	Record Length (Days)	ADCP (kHz)	Sample Depth (m)	Sample Interval (min)
Moorings 1	96.2	114°54.4'	21°21.9'	2006.12.8–2007.2.5	60	300	8.0–84.0 $\Delta z = 4$ m	10
Moorings 2	105.9	115°10.2'	21°8.5'	2006.12.8–2007.2.5	60	300	9.0–93.0 $\Delta z = 4$ m	10
Moorings 3	287.1	115°42.1'	20°51.3'	2006.12.8–2007.2.5	60	150	53.0–269.0 $\Delta z = 8$ m	10
Moorings 4	205.0	115°0.2'	20°14.2'	2009.12.10–2010.4.2	114	150	18.0–186.0 $\Delta z = 8$ m	10
Moorings 5	784.0	115°14.1'	20°4.6'	2009.12.10–2010.4.2	114	75	59.0–459.0 $\Delta z = 16$ m	30
Moorings 6	1829.0	115°30.4'	19°43.4'	2009.12.10–2010.4.2	114	75	51.0–467.0 $\Delta z = 16$ m	30
Moorings 7	261.0	117°11.4'	21°44.3'	2009.12.24–2010.3.24	90	150	50.0–242.0 $\Delta z = 8$ m	10
Moorings 8	127.0	118°8.5'	22°12.1'	2009.12.24–2010.3.24	90	300	38.0–114.0 $\Delta z = 8$ m	10

mounted at a depth of 500 m with an aim at measuring currents in the upper 500 m layer. Three types of frequencies were set up, with a bin length of 4 m for 300 kHz ADCP, 8 m for 150 kHz ADCP, and 16 m for 75 kHz ADCP. The sample interval was 10 min for 150 kHz and 300 kHz ADCPs and 30 min for 75 kHz ADCPs. All moorings were recovered successfully with record lengths of approximately 60 days at M1–M3, 114 days at M4–M6, and 90 days at M7–M8. A 3 h low-passed Lanczos filter was used to convert the current records to an hourly interval [Chen *et al.*, 1996].

During the winter 2009 deployment cruise, a hydrographic survey was conducted during 16–31 January 2010, with CTD profile data being collected in a 1 m vertical sampling bin at 58 stations (Figure 1). Two meteorological buoys (B1 and B2) were deployed around the 50 m isobaths in 2002 and 2005, respectively, with an aim at monitoring the wind over the NSCS continental shelf. The wind speed and direction were recorded at 30 min intervals on these two buoys with full data coverage during the 2006–2007 and 2009–2010 mooring deployments. The same 3 h low-passed Lanczos filter was used to resample the wind records to hourly intervals. Satellite-derived Maps of Absolute Dynamics Topography (MADT) were used to track an eddy that was detected in the moored current data. The MADT product was obtained from the Archiving, Validation and Interpretation of Satellite Oceanographic (AVSIO) database with a spatial resolution of $1/4^\circ \times 1/4^\circ$ and a time interval of 7 days.

2.2. The Model

The primitive equation, unstructured-grid, Finite-Volume Community Ocean Model (FVCOM) was used to interpret the features of the internal tidal currents observed at the moorings. FVCOM was developed originally by Chen *et al.* [2003] and continuously improved and updated by the joint research team at the University of Massachusetts-Dartmouth and Woods Hole Oceanographic Institution [Chen *et al.*, 2006a, 2006b, 2013]. This model was configured for the South and East China Seas with a horizontal resolution varying from 1–4 km in the inner shelf and over the slope to ~ 35 km near the open boundary in the NSCS continental shelf region [Chen *et al.*, 2012]. A hybrid terrain-following coordinate was used in the vertical, with a total of 40 layers and the coordinate transition at the 80 m isobath. In the region of >80 m, the s -coordinate was adopted, which featured five uniform layers with a layer thickness of 2 m from the surface and bottom, respectively. In the region of <80 m, the σ -coordinate with uniform layer thickness in the vertical was applied. This uniform layer thickness was 2 m at the transition and smaller as the water depth became shallower. This hybrid coordinate was designed to resolve the surface and bottom boundary layers with a vertical resolution of at least 2 m or less. Chen *et al.* [2012] named this regional model “the China coastal FVCOM.” Hereafter we refer to it as “CC-FVCOM.”

We used CC-FVCOM to simulate the barotropic and baroclinic tides under homogenous and January climatological stratification conditions [Chen *et al.*, 2012]. In these experiments, the vertical eddy viscosity and horizontal diffusion coefficients used in the model were calculated by Mellor and Yamada level 2.5 (MY-2.5)

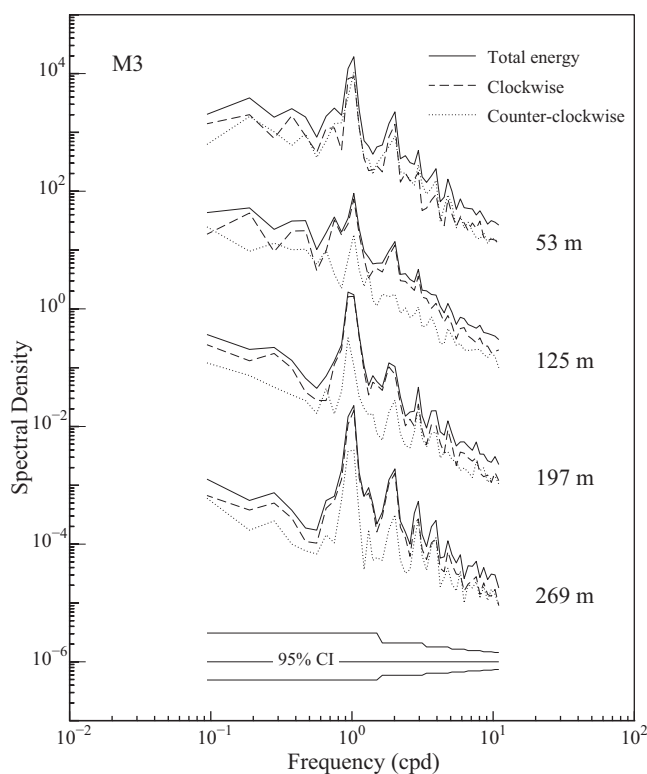


Figure 2. Rotary spectra of currents measured at depths of 53, 125, 197, and 269 m at M3. Solid line: the total energy; dashed line: the clockwise energy; and dot line: the counter-clockwise energy. The spectra at depths of 125, 197, and 269 m were shifted downward by 10^2 , 10^4 , and 10^6 , respectively. Power spectrum density (psd) is in $(\text{cm/s})^2/\text{cpd}$.

and Smagorinsky turbulent closure schemes, respectively [Mellor and Yamada, 1982; Smagorinsky, 1963]. The tidal forcing on the open boundary was specified by the amplitudes and phases of the five major tidal constituents (three semidiurnal: M_2 , S_2 , and N_2 ; two diurnal: O_1 and K_1). The model was integrated for 55 days, and the hourly model output after 10 spin-up days was used for tidal harmonic analysis. The bathymetric data used in the model were taken from combined 2 min Naval Oceanographic Office Digital Bathymetric Data Base-Variable resolution (DBDBV) and Chinese bathymetric charts. Since the model bathymetry did not match very accurately with the true water depths recorded at the moorings, our model-data comparison was focused only qualitatively on the vertical and spatial distributions of the internal tidal currents.

3. Spatial Structure of Internal Tidal Currents

3.1. Observational Results

Current records at eight moorings clearly showed that tidal currents were predominant over the NSCS continental shelf. Rotary spectral density was characterized by the two peaks at diurnal (O_1 and K_1) and semidiurnal (M_2 and S_2) frequency bands, respectively, even though the tidal energy distribution varied significantly in space. Figure 2 presents an example of the spectral density distributions at depths of 53, 125, 197, and 269 m on M3. Both diurnal and semidiurnal tidal energies increased with depth, while tidal energy was much stronger in the diurnal frequency band than in the semidiurnal frequency band. As the depth deepened, the clockwise-rotating energy was much higher than the counterclockwise-rotating energy, indicating that tidal currents primary rotated clockwise at this mooring site. This feature was also seen at the other seven moorings, suggesting that this was a general feature over this shelf. The diurnal and semidiurnal tidal energy densities varied significantly in both cross-shelf and along-shelf directions (Figure 3). For the K_1 tidal constituent, on the M1-M3 cross-shelf transect, the M3 energy (near the 300 m isobath) was intensified near the surface and bottom. This feature was still seen at M2 (around the 100 m isobath), but not at M1 (around the 90 m isobath). At M1, the energy was relatively uniform through the water column and then decreased monotonically near the bottom. On the M4-M6 transect, the energy at M5 (near the 800 m isobaths) showed a similar energy distribution pattern as that at M3, but over about a 30 km distance, the energy either decreased monotonically with depth at M6 or was subsurface-intensified at M4. Combining M4, M3, M7, and M8 to form an along-shelf transect, the vertical distribution of the diurnal tidal energy on this transect also significantly differed at these four mooring sites. For the M_2 tidal constituent, at M3, its energy exhibited a vertical distribution similar K_1 , but it was subsurface intensified at M7 and bottom intensified at M4 and M8.

Harmonic tidal analysis using T_TIDE [Pawlowicz *et al.*, 2002] was conducted to examine the vertical and spatial distributions of the diurnal and semidiurnal tidal current ellipses. Figure 3 shows a direct view of the

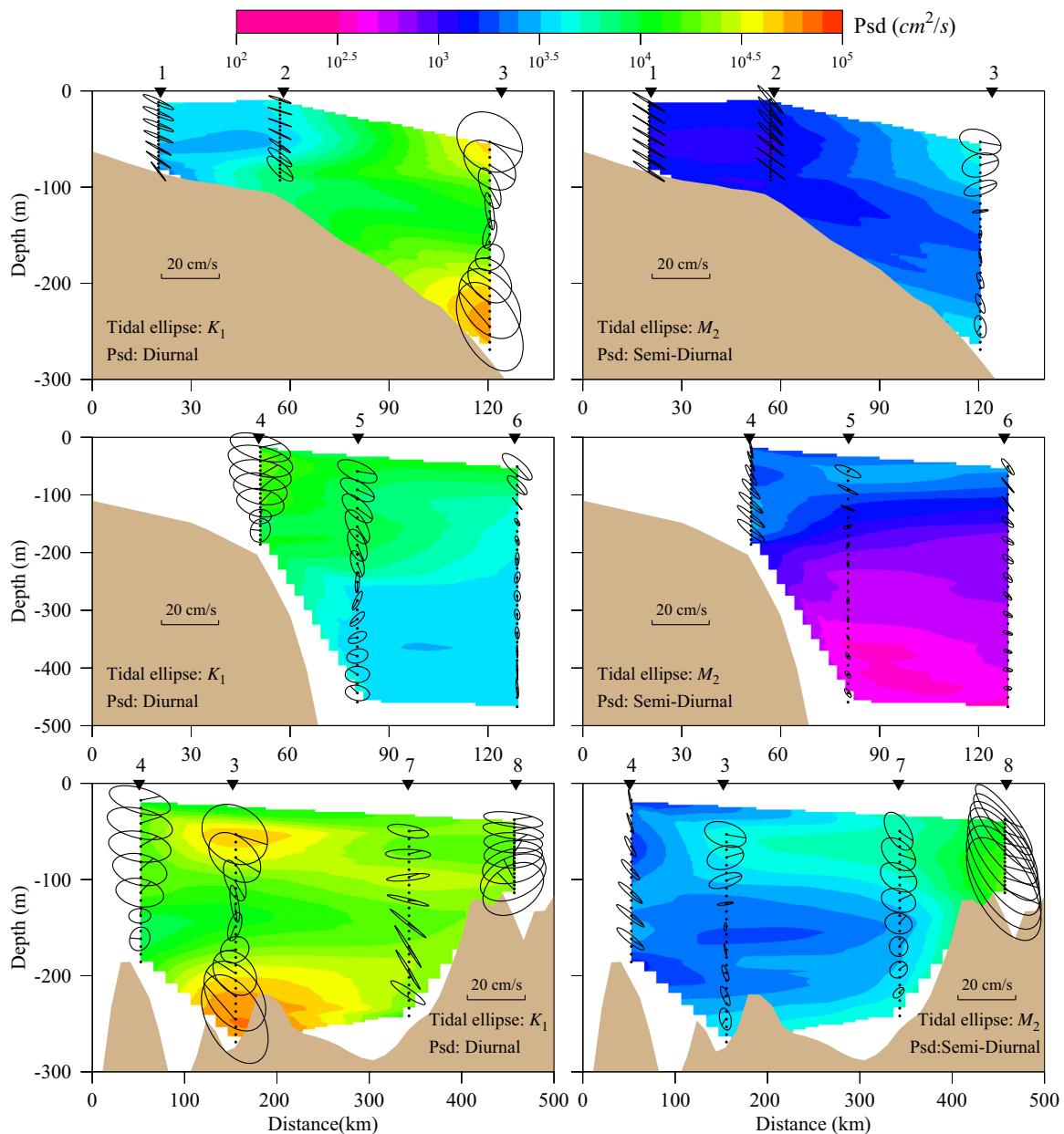


Figure 3. Contours of power spectra density (psd) at diurnal and semidiurnal frequencies (color images) superposed with tidal current ellipses (slide line ellipses) on transect of M1-M3, M4-M6, and M4-M3-M7-M8, respectively.

ellipse amplitudes and phases of the major constituents (K_1 and M_2). At M3, the K_1 tidal current was surface and bottom intensified, with amplitudes of 12.7 and 16.7 cm/s near the surface and bottom, respectively. A 180° phase difference was observed in the upper and lower layers, with a transition around the depth of 165 m at which the K_1 tidal current reached its minimum amplitude of 4.7 cm/s. This is a characteristic feature of internal tidal waves, as described in previous studies [Duda and Rainville, 2008; Guo et al., 2012; Xu et al., 2013]. This feature, however, was not observed at M4 at the shelf break, where significant changes of K_1 tidal current amplitude and phase only occurred in the bottom boundary layer, and no opposite phase between the upper and lower layers existed. Over most of the shelf, the K_1 tidal currents were dominant except at M8 where the M_2 tidal currents were stronger. A stronger M_2 tidal current at M8 was believed due to the interaction of the M_2 tidal currents with steep bottom topography as the M_2 tidal waves from Luzon Strait and Taiwan Strait propagated onto the shelf. The internal tidal features are predominant over the

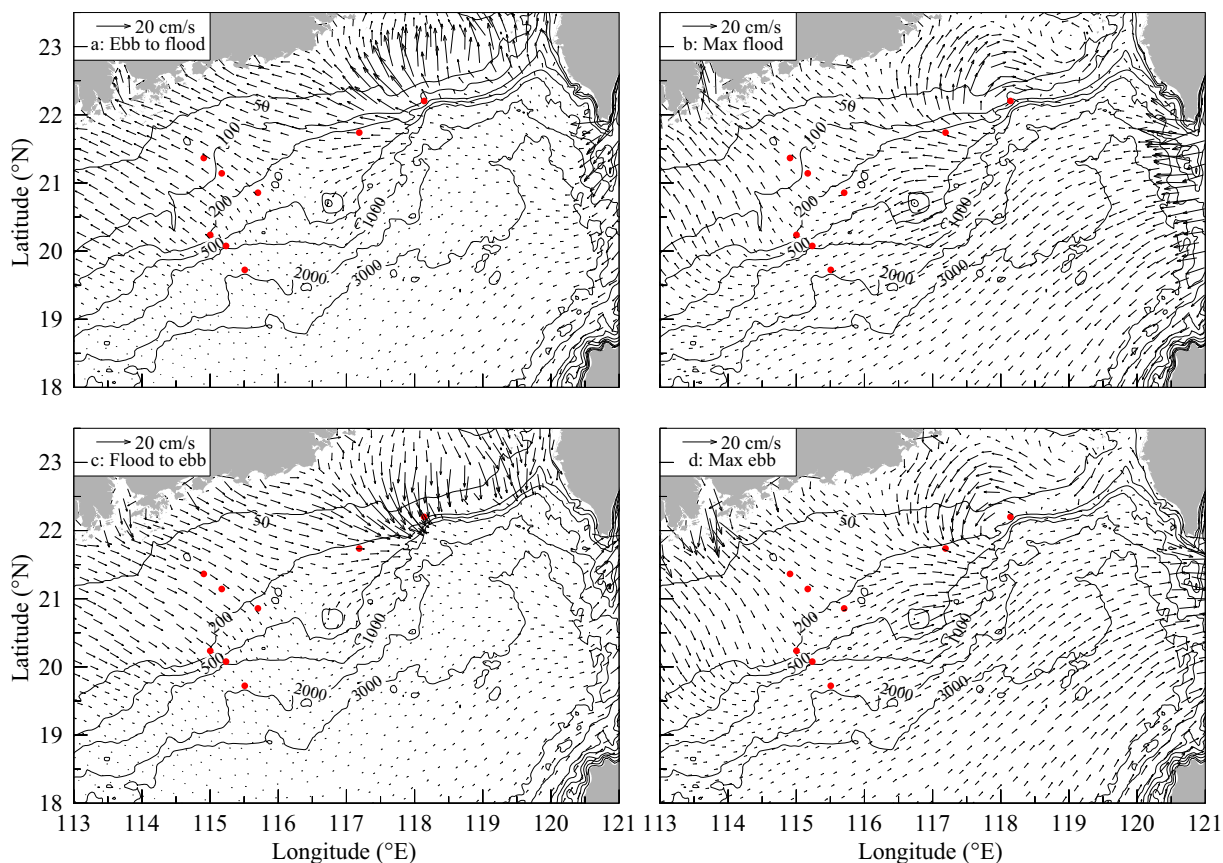


Figure 4. Distributions of the model-predicted vertically averaged barotropic K_1 tidal current vectors at the transition from ebb to flood, maximum flood, from food to ebb, and maximum ebb. Red dots: locations of moorings.

shelf break and decreased toward the coast. In the winter season, the water in the shelf region of <70 m was vertically well mixed. This was the reason why internal tidal signals were weak at M2 and disappeared at M1. Similarly at M7 and M8, on the northeast of Dongsha Island, the vertical shears of tidal currents were relatively smaller compared with other stations, even though both M_2 and K_1 tidal currents were stronger in the lower water column.

The key finding here is that both barotropic and baroclinic tidal currents varied significantly in space. Even separated along similar isobaths within a distance of ~ 100 km, the structure of the tidal current could be very different. The surface and bottom intensification with a 180° phase difference in the vertical, which were reported in previous tidal studies [Xu *et al.*, 2013], were clearly localized and did not represent the general internal tidal features over the NSCS shelf.

3.2. Process-Oriented Tidal Model Experiment Results

What were the dynamics controlling the spatial variability of tidal currents over the NSCS shelf? To address this question, we examined the CC-FVCOM-generated tidal current fields over the NSCS shelf for both barotropic and baroclinic cases. For the baroclinic case, the model ran prognostically with initial conditions of the temperature and salinity specified using the January climatologically averaged hydrographic fields. We focused our discussions on the K_1 tidal currents here, because it was predominant over this shelf. In the barotropic case, when the K_1 tidal wave, which entered the SCS from Luzon Strait, arrived on the NSCS shelf, it split into two branches: one first propagated southwestward along the slope and then turned clockwise to enter the NSCS shelf around M1-M3, and another rotated clockwise between M7 and M8 (Figure 4). This pattern reversed during the ebb tidal periods. The speed and direction of the model-produced K_1 tidal current remained little change in the vertical except decreased rapidly in the bottom boundary layer, which

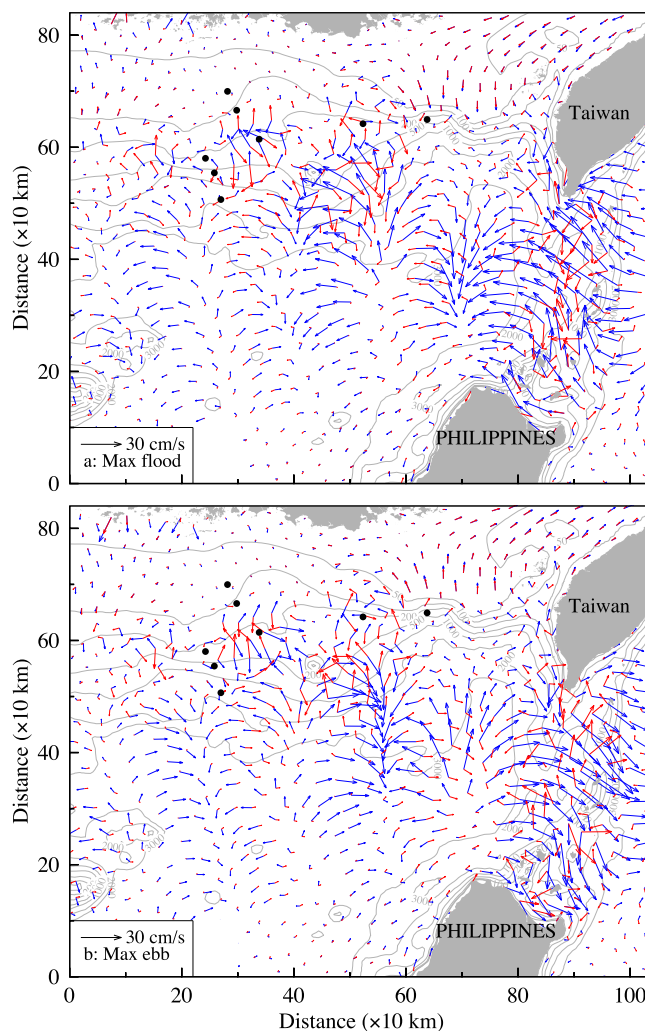


Figure 5. Distributions of the model-predicted K_1 internal tidal current vectors near the surface (red) and bottom (blue) at maximum flood and ebb. The CC-FVCOM was driven by the tidal forcing at the nesting boundary with the initial conditions specified with the January climatology of the sea temperature and salinity. The figures were rotated clockwise by an angle of 26° .

was relatively strong, with anticyclonic and cyclonic rotating over the flood and ebb tidal periods, respectively.

When stratification was added, the K_1 tidal current in the NSCS shelf can be characterized as a baroclinic Kelvin wave propagating along the isobaths over the slope with a wavelength of about 300 km and a cross-shelf internal Rossby radius scale of 100–200 km [Kelvin, 1879; Rhine, 1967, 1969a]. The vertical structure of this tidal wave was characterized by the first mode with a reversed flow direction in the upper and lower layers (Figure 5). The phase difference of the tidal current in the vertical varied in different flow zones. M3 was located around the maximum tidal current magnitude zone where the phase difference of the tidal current near the surface and bottom was about 180° (Figure 5). M4 was around the transition zone between clockwise and counterclockwise tidal currents, where the tidal flow was relatively weak, and the vertical phase difference was only about 90° . The model-predicted phase of the baroclinic K_1 tidal flow field was in good agreement with the observation at M3 (Figure 6), even though at this site the water depth used in the model was about 20 m deeper than the observed depth. The model results suggested that the spatial variability of tidal currents observed at the mooring sites were the feature of internal tides generated by the baroclinic Kelvin waves. For this reason, the interpretation of tidal measurements needs to be made with caution to avoid an inaccurate conclusion made just based on measurements on a single mooring.

was similar to the results described in Fang *et al.* [1999]. The magnitude of the vertically averaged tidal current varied significantly in space and over bathymetry. The shelfbreak area, particularly along the 200 m isobaths between M3 and M4, featured a divergence zone during the flood tidal period and a convergence zone during the ebb tidal period (Figure 4). From ebb to flood, the tidal current was oriented westward along the isobaths over the slope but turned to the cross-isobath direction over the shelf in the region less than 200 m. This pattern remained little changed during the flood tidal period, while the along-isobath southwestward tidal current increased with time and reached its maximum at the maximum flood tide. The direction of the tidal current reversed at the transition from flood tide to ebb tide, with a relatively strong offshore tidal flow over the shelf and an along-isobath northeastward tidal flow over the slope. This pattern remained unchanged as the along-isobath northeastward tidal flow increased during the ebb tidal period.

Around M8, the tidal current

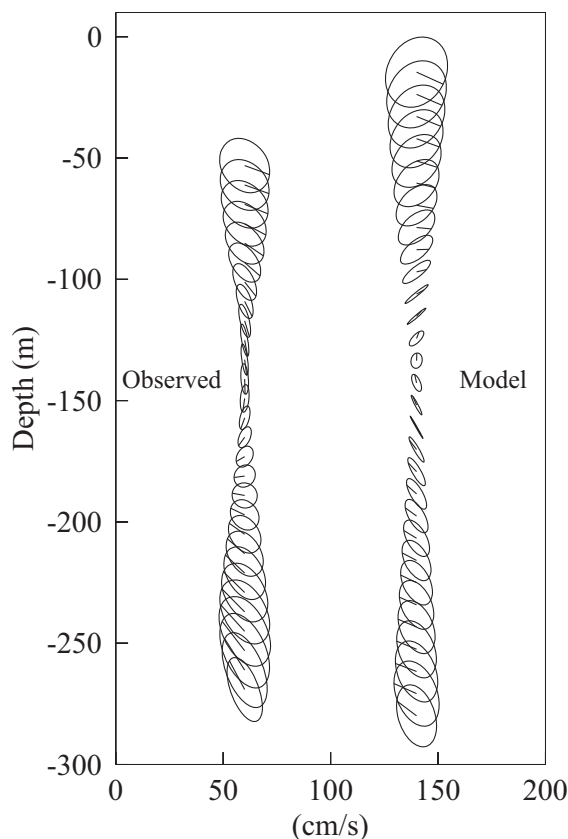


Figure 6. Comparisons of observed and model-computed vertical distributions of the K_1 internal tidal current ellipses at M3.

4. Subtidal Currents

4.1. Monthly Averaged Flow Fields

The subtidal flow is defined here as the low-pass filtered currents at a cutoff frequency of 33 h. The filter used in this study was the pl66tn described by *Beardsley and Rosenfeld* [1983]. The same filter was used for the wind data recorded on buoys 1 and 2 (B1 and B2) to create the low-frequency wind velocity for the same time interval as the subtidal flow. The distance between B1 and B2 was about 200 km. Since the spatial scale of the wind was much larger, no significant difference was found in the wind records at these two buoys. For this reason, we used the wind velocity on the closer of the two buoys when we described the subtidal flow and its correlation with the wind.

Controlled by the NE monsoon, northeasterly winds prevailed over the NSCS shelf during the winter season, stronger in 2006–2007 than in 2009–2010. Over the NSCS shelf, the along-isobath southwestward flow was dominant during the winter season for both 2006–2007 and 2009–2010. For example, Figure 7 shows the B1 wind and M3 current vector time series for the 2006–2007 winter season. With strong NE winds (mean ~ 8.6 m/s), the currents at 53 and 125 m were predominantly flowing toward the southwest and west with means of ~ 20 and ~ 10 cm/s, respectively (Table 2). On the M1–M3 transect, the monthly averaged along-isobath subtidal current was southwestward and surface-intensified, with a maximum speed of ~ 20 cm/s in December 2006 and January 2007 (Figure 8, left). The

Controlled by the NE monsoon, northeasterly winds prevailed

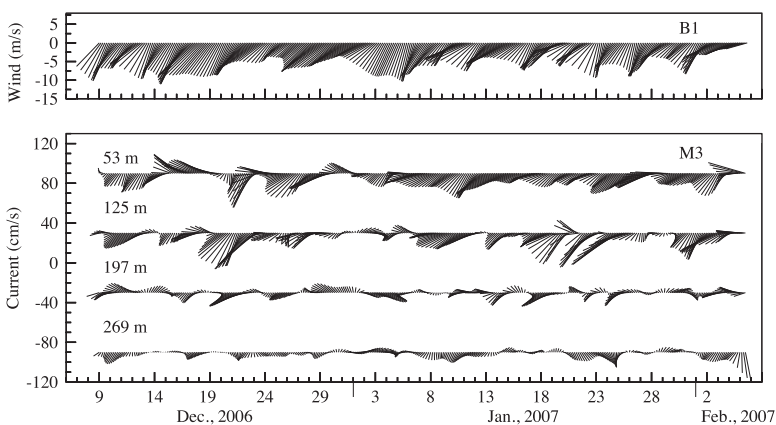


Figure 7. Time series of the 33 h low-pass filtered (top) wind and (bottom) current vectors on buoy B1 (for winds) and M3 (for currents) at depths of 53, 125, 197, and 269 from 6 December 2006 to 5 February 2007.

Table 2. Statistics of Observed Subtidal and Wind Velocities at Moorings and Buoys^a

Station	Depth(m)	U (cm/s)		V (cm/s)		Speed (cm/s)	Direction (°)
		Mean	Std	Mean	Std		
M1	11	-17.2	11.1	-7.9	7.5	18.9	246
	35	-9.1	13.1	-3.1	8.1	9.6	251
	59	-8.7	13.1	-3.0	8.1	9.2	251
M2	83	-8.4	13.0	-2.9	8.0	8.9	251
	8	-19.3	14.1	-7.1	10.8	20.5	250
	36	-17.9	13.2	-6.7	10.1	19.1	249
	64	-17.6	13.1	-6.7	10.0	18.8	249
M3	92	-17.2	12.9	-6.7	9.9	18.5	249
	53	-17.3	19.0	-8.8	20.3	19.4	243
	125	-17.6	18.3	-9.3	19.8	19.9	242
M4	197	-18.1	17.6	-9.7	19.2	20.5	242
	269	-18.5	17.0	-9.8	18.7	21.0	242
	17	-18.9	16.5	-6.4	17.4	20.0	251
	73	-9.0	18.5	-4.6	14.9	10.1	243
M5	129	-9.2	18.1	-4.8	14.9	10.4	242
	185	-9.6	17.5	-5.1	14.7	10.9	242
	59	-4.5	18.1	-4.5	17.1	6.3	225
	187	-6.4	16.5	-4.9	16.2	8.1	233
M6	315	-7.9	15.5	-6.0	15.7	9.9	233
	459	-8.7	14.5	-7.3	14.6	11.4	230
	51	1.0	29.5	2.9	25.0	3.1	18
	179	-0.5	28.8	2.5	23.7	2.5	349
M7	323	-1.1	26.0	1.6	22.0	1.9	326
	467	-1.5	22.6	0.7	20.3	1.7	294
	49	-9.9	22.5	0.7	18.4	9.9	274
	113	-10.8	22.2	0.3	17.7	10.8	271
M8	177	-11.9	22.1	-0.2	17.4	11.9	269
	241	-12.5	22.1	-0.3	17.0	12.5	269
	37	-6.2	25.1	-0.1	16.9	6.2	269
	61	-6.2	24.7	-0.6	16.8	6.3	264
B1-06-07 (m/s)	85	-6.3	24.2	-1.2	16.8	6.4	260
	109	-6.5	23.6	-1.7	17.0	6.7	255
	B1-09-10 (m/s)	-6.3	3.1	-2.1	2.5	6.7	72
B2-09-10 (m/s)	-5.8	3.2	-1.3	3.3	5.9	78	

^aNote: M1-M8: currents; B1-B2: winds. 06-07 and 09-10 denote 2006-2007 and 2009-2010.

flow was relatively uniform in the upper 100 m, where the water was vertically well mixed. In December 2006, the cross-isobath flow was characterized by secondary double circulation cells over the slope: an onshore flow in the upper water column, an offshore flow in the lower water column and near the bottom, and an onshore flow near the bottom in the deep slope (Figure 8, top right). In January 2007, flow in the lower water column and near the bottom was offshore (Figure 8, bottom right). The southwestward flow pattern remained unchanged during the winter of 2009-2010. On the M4-M6 transect, the monthly averaged flow in the upper 500 m were all southwestward during December 2009 through March, 2010 (Figure 9, left). The monthly averaged along-isobath flow was surface-intensified in December, with a maximum velocity of ~27.5 cm/s; subsurface-intensified in January, with a maximum velocity of ~20 cm/s at a depth of

150 m; and bottom-intensified in February and March, with maximum velocities of ~17.5 and ~10 cm/s, respectively. In the cross-isobath direction, the flow was onshore and surface-intensified, with a maximum velocity of 15 cm/s in December; onshore in the upper 100 m layer and offshore in the lower layer, with an inflow and outflow velocity of ~2.5 cm/s in January; and onshore and offshore in the upper 500 m layer, with a maximum velocity of ~15 cm/s in February and March, respectively (Figure 9, right).

The observed along-isobath southwestward flow was generally consistent with the cross-isobath distribution of the satellite altimeter-derived sea surface height (SSH) during the winters of these 2 years except in February and March 2010 (Figure 10). In December 2006, the monthly averaged SSH was higher at M1 and decreased offshore, with a cross-isobath gradient of $\sim 6 \times 10^{-7}$ over a distance from M1 to M3. This gradient could produce an along-isobath southwestward geostrophic velocity of ~11 cm/s. Considering a 30 km spatial resolution and uncertainties in the altimeter data, the SSH-derived geostrophic flow was in the same order of the observed surface current at these three moorings. This cross-isobath SSH pattern remained unchanged in January 2007, but the gradient was much smaller. The cross-isobath distribution of SSH on the M4-M6 transect in December 2009 was very similar to that on the M1-M3 transect in December 2006. The SSH gradient over a distance from M4 to M6 was 10.3×10^{-7} , which resulted in an along-isobath geostrophic velocity of ~21 cm/s. In January 2010, the negative (decreasing offshore) SSH gradient was only over the shelf where the water depth was shallower than 200 m, while it slightly increased from M4 to M6. This was also consistent with the current measurement data, which showed a weak near-surface northeastward flow at M6. In February, 2010, however, no significant cross-isobath SSH gradient was measured, suggesting that the subsurface-intensified southwestward flow was driven by baroclinic processes in addition

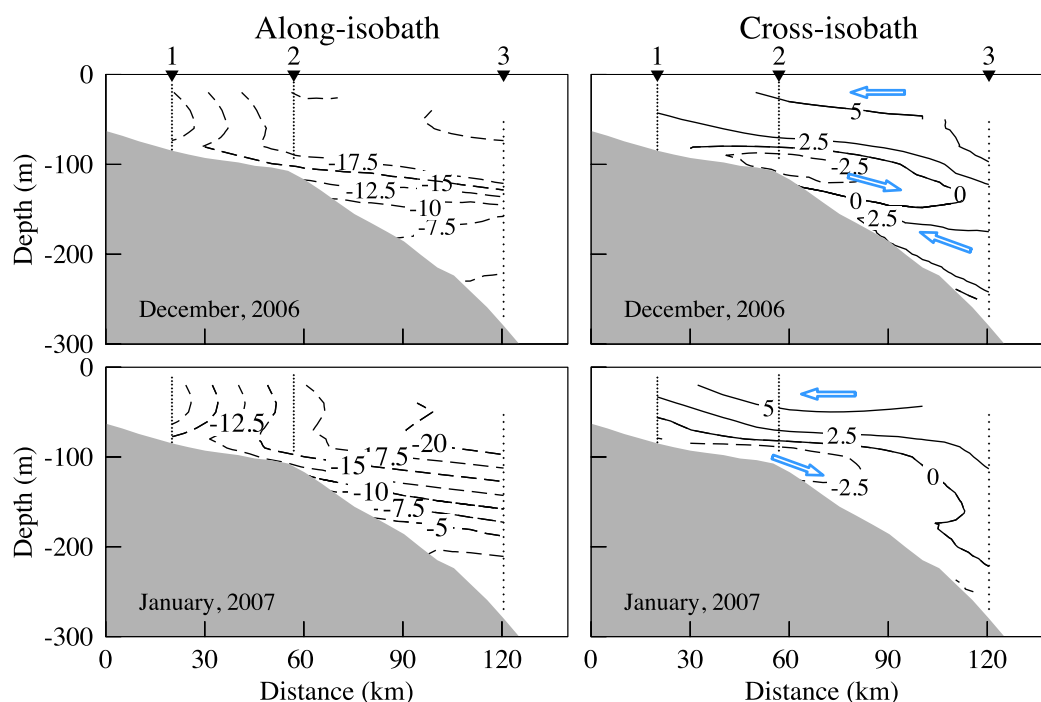


Figure 8. Distributions of monthly averaged (left figures) along-shelf and (right figures) cross-shelf velocities on transect M1-M3 for December 2006 and January 2007.

to the wind forcing. In March, 2010, a surface-intensified northeastward flow with a maximum velocity of ~ 10 cm/s was observed in the upper 100 m layer between M5 and M6, which was consistent with the positive SSH gradient between these two stations.

The monthly averaged observed currents and SSH were consistent with wind-driven Ekman flow theory. The downwelling-favorable NE wind stress produced an onshore Ekman transport in the upper layer. The resulting negative gradient of the sea surface elevation, formed as a result of the water piled up onshore, pushed water offshore in the lower layer, and turned clockwise to balance with the Coriolis force. When a quasi-equilibrium state was reached with a balance between the Coriolis and cross-isobath pressure gradient forcing, an along-isobath southwestward flow formed. The onshore Ekman transport in the upper layer also produced an offshore water transport in the lower layer or near the bottom as a result of volume conservation. All these features appeared consistently in the moored current measurements. This fact implied that on a monthly averaged time scale, the low-frequency subtidal flow over the NSCS shelf was mainly wind-driven.

4.2. The Eddy Flow Field

Although the wind-induced circulation was dominant in the 2006–2007 and 2009–2010 winters, the moored current records clearly showed episodic events of mesoscale eddies that passed the measurement sites during those periods. On 30 December 2009, the daily altimeter sea surface height (SSH) image identified an anticyclonic eddy with a radius of ~ 100 km near the southwestern coastal region of Taiwan (Figure 11). This eddy moved southwestward at a speed of ~ 9.4 cm/s, passed M8 around 13 January 2010, M7 around 27 January 2010, and M5-M6 around 10 March 2010. The movement of the eddy was guided by the Rossby wave with a westward propagation phase speed of $9\text{--}10 \pm 3$ cm/s around latitudes of $18^\circ\text{N}\text{--}22^\circ\text{N}$ [White, 2000; Wang *et al.*, 2008].

The vertical profile of this eddy was captured well in current records on these mooring sites. The current on M8 turned northeastward against the NE wind on 5 January and remained in this direction until 23 January, during which the northern portion of the anticyclonic eddy passed (Figure 12). This northeastward eddy velocity dominated throughout the whole water column, with a swirl velocity up to $\sim 30\text{--}40$ cm/s at a depth of 37 m and ~ 10 cm/s at a depth of 109 m near the bottom. When the eddy was located around M8, its

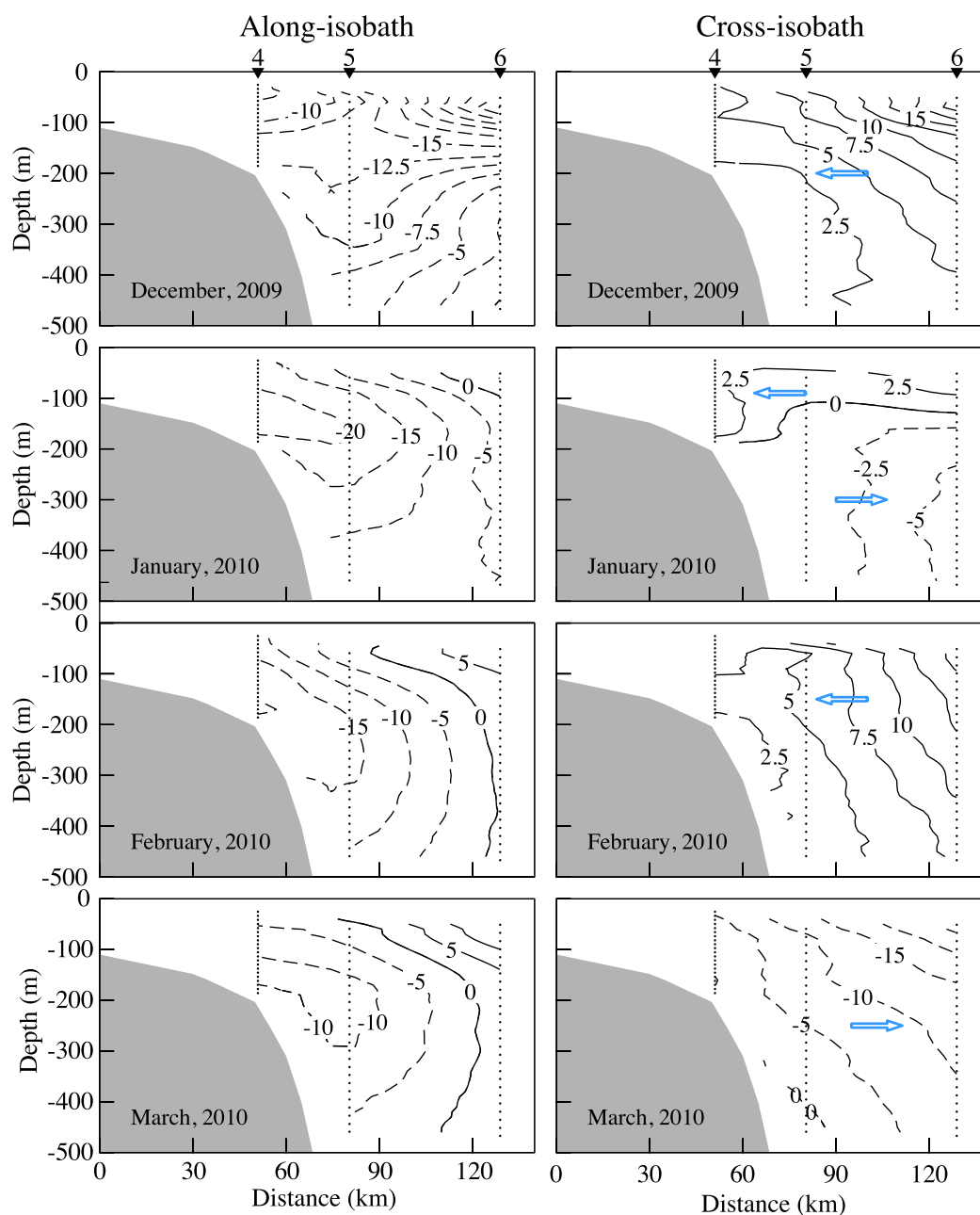


Figure 9. Distributions of monthly averaged (left figures) along-shelf and (right figures) cross-shelf velocities on transect M4-M6 for December 2007 and January, February, and March, 2007.

edge had affected the flow field around M7, located about 110 km southwest of M8. During that period, the current at M7 was dominated by a northwestward flow in the upper 200 m layer, with a velocity of ~ 15 cm/s at a depth of 49 m (Figure 12). This northwestward flow did not exactly follow the SSH contour, suggesting that it was a result of the combined wind and eddy-driven circulations (Figure 11). The northwestern portion of the eddy passed M7 on 24–28 January, during which the current at that site was dominated by a surface-intensified northeastward flow with a velocity of ~ 40 cm/s at a depth of 49 m and a vertical scale of ~ 200 m. As the eddy moved southwestward following the 500–1000 m isobaths, it continued to affect the flow field at M7 until 13 February, where the current turned eastward and southward following the change in the location and shape of the eddy. Similarly, when the center of the eddy passed M6 on its south along the 500–1000 m isobaths, the velocity on M6 had been affected by the eddy in late February (Figure 13). A strong northeast velocity of ~ 50 – 70 cm/s was recorded at a depth of 51 m during

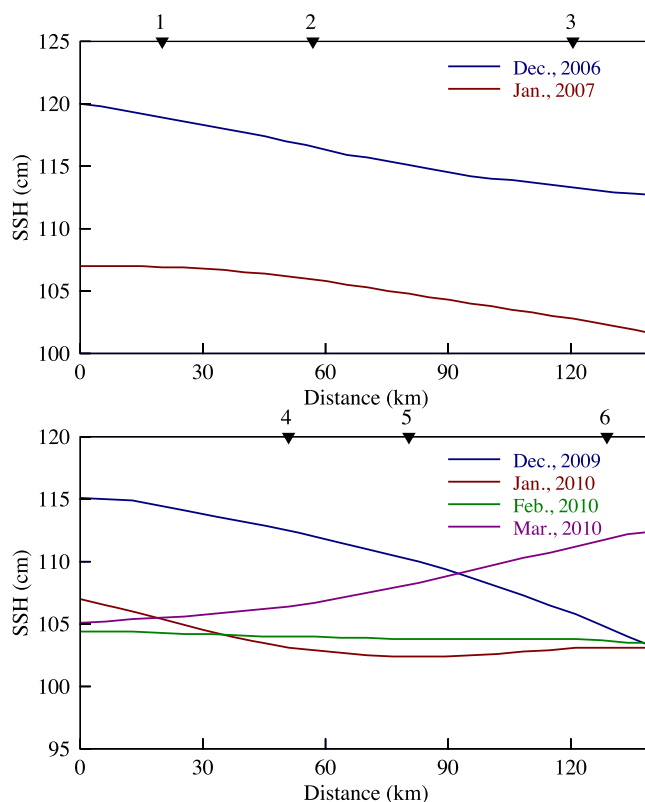


Figure 10. Cross-shelf (solid line in Figure 1) distributions of the monthly averaged satellite-derived altimeter sea surface height (SSH) (unit: cm) on M1-M3 (for December 2006 and January 2007) and on M4-M6 (for December 2009 and January, February, and March, 2010).

surface geostrophic velocity, which was estimated by the altimeter SSH, was about ~ 60 cm/s, which is in the same order of magnitude recorded at M6.

4.3. Wind-Current Coherences Analysis Results

The moored current records clearly showed that without considering the influence of mesoscale eddies, subtidal currents over the NSCS shelf during the winter season were dominated by the southwestward upper water column flow that was driven mainly by the NE wind. To further test this conclusion, we conducted a correlation analysis between the southwestward component of the near-surface subtidal current and the wind with a direction range of -180° to 180° . The correlation values at M1-M3, for example, all exceeded 0.85 with the critical value of 0.29 at a 95% confidence level (Figure 15). Since the NE wind was dominant over the NSCS shelf during the 2006–2007 and 2009–2010 winters, the highest correlation values occurred with the wind-current angle between -60° and 60° and covered the entire time scale over the winter season. The current records at M7, M8, and M5-M6 clearly demonstrated that the flow field over the NSCS shelf was influenced significantly by mesoscale eddies. Since the observed eddy moved southwestward at a relatively constant speed related to the westward propagation speed of Rossby waves, the influence of an eddy on the local current occurred over a time scale of about a week. Because of the existence of these eddies, the wind-current correlation was reduced. The correlation value at a depth of 17 m at M4 was >0.8 , but was reduced to 0.5 at a depth of 59 m at M5 and to 0.1 at a depth of 51 m at M6 (Figure 16). The correlation value at M6 was smaller than the critical value of 0.21 at a 95% confidence level. It was clear that the correlation value became smaller as the distance to the center of the eddy was decreased (Figure 11). Similar results were also reported at M7 and M8. The correlation value was 0.5 at a depth of 49 m within the direction range of 0° – 45° at M7 and only 0.2 at a depth of 37 m at M8. When the current records during the passage of the anticyclonic eddy were removed, the correlation at these two stations increased to ~ 0.8 .

The lowest correlation value found at M6 was not only due to the passage of the anticyclonic eddy. During the period 10–30 January 2010, the velocity at a depth of 51 m at M6 was in an opposite direction to the wind (Figure 13). In the vertical, the flow was characterized by a first baroclinic mode, with northeastward

20 February through 5 March, due to a combination of wind- and eddy-driven flows. The velocity at M6 was still dominated by the eddy flow until the end of March 2010, during which the current rotated clockwise from the northeast direction to the south direction as the eddy passed during the period of NE wind (Figure 13).

A CTD survey was conducted on the NSCS shelf during 16–31 January 2010, during which vertical profiles of temperature and salinity were measured at 56 stations (Figure 1). Fortunately, the eddy was captured on transect S4 during 30–31 January (Figure 14). The transect data showed this eddy was a typical warm-core anticyclone with concave across-eddy temperature and salinity distributions and raised sea surface height (determined by altimeter SSH). This eddy had a cross-isobath scale of 100–150 km and a vertical scale of about 400 m. The

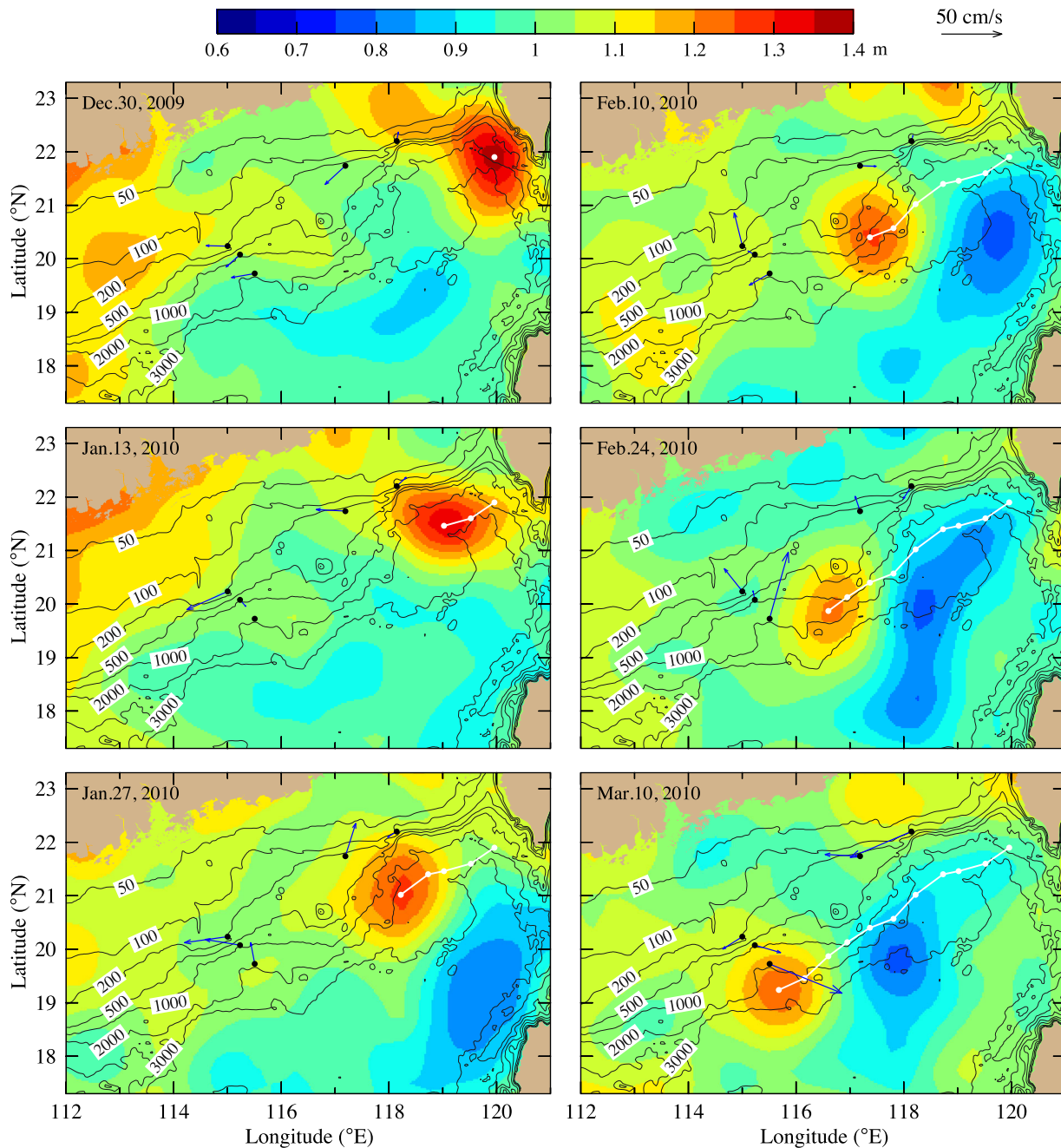


Figure 11. Snapshots of satellite-derived altimeter SSH images over 7 day intervals starting on 30 December 2009. The white line was the trajectory of the anticyclonic eddy with dots indicating its location over 7 day intervals. The blue vectors are the near-surface velocity observed on mooring at the time that the images were plotted.

flow in the upper 51 m and a deep-intensified southward flow beneath 179 m. There was no well-defined eddy passing this site during that period, suggesting that other buoyancy-related mechanisms in addition to the wind and eddy existed over the NSCS slope.

5. Discussion

The moored current measurements during the 2006–2007 and 2009–2010 winters suggested that the wintertime circulation over the NSCS was characterized by the wind-induced southwestward flow plus an

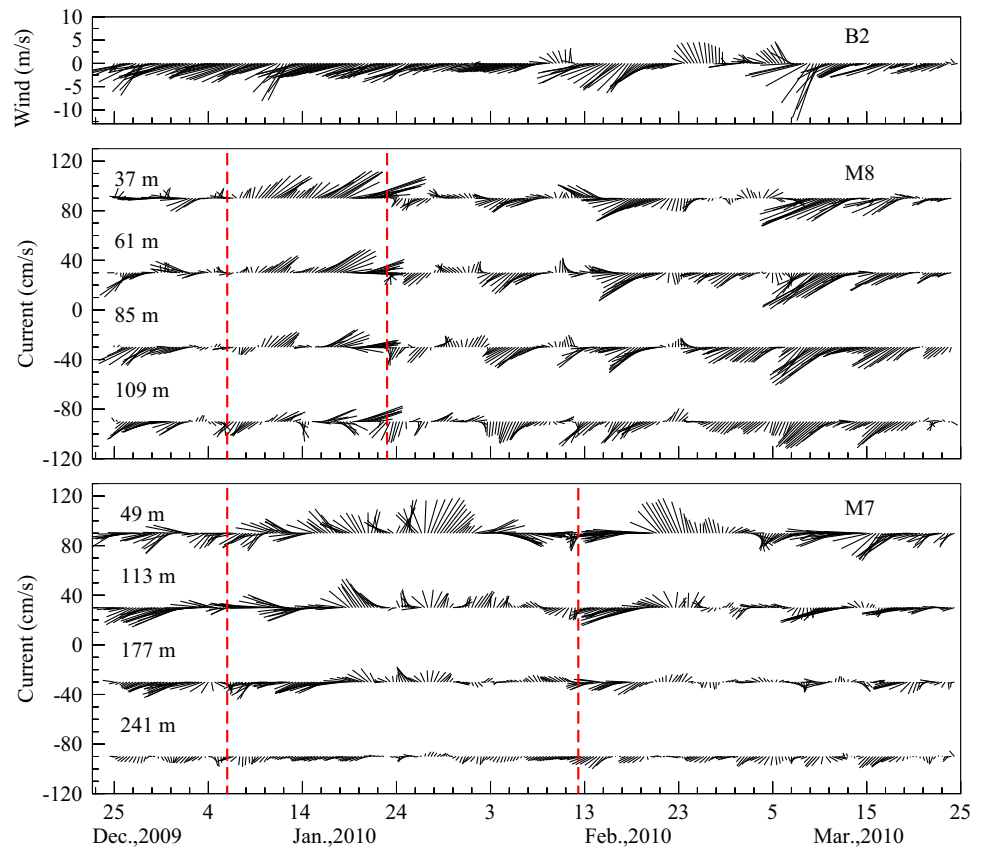


Figure 12. Time series of the 33 h low-pass filtered (top) wind and (bottom) current vectors on buoy B2 (for winds), on M8 (for currents) at depths of 37, 61, 85, and 109 m, and on M7 (for currents) at depths of 49, 113, 117, and 241 m over the time periods from 24 December 2009 to 25 March 2010.

episodic influence of mesoscale eddies. This finding differs from the early conceptual wintertime circulation pattern proposed by Guan and Chen [1964] and Guan [1978], who believed that the northeastward buoyancy-driven SCSWC was the dominant wintertime current feature between the 200 and 400 m isobaths over the NSCS shelf. The SCSWC was defined by the geostrophic flow computed from hydrography using the bottom as the level of no motion (LNM). We did not detect the SCSWC in our moored current measurements during the two winter deployments. We next calculated the along-isobath geostrophic velocity based on the 16–31 January 2010 hydrographic survey using the bottom as the LNM in the region shallower than 1000 m and equal to 1000 m in deeper water. On the M1-M3 transect, for example, the vertical geostrophic velocity shears

showed similar trends compared to the observed velocity shears below 20 m, even though the values differed significantly (Figure 17, top). A bottom-intensified southwestward along-isobath flow of ~10–15 cm/s was observed near the bottom at M1, quite different that the small northeastward geostrophic velocity computed with the bottom as LNM (Figure 17, bottom). When the observed velocity at 60 m was added as the reference

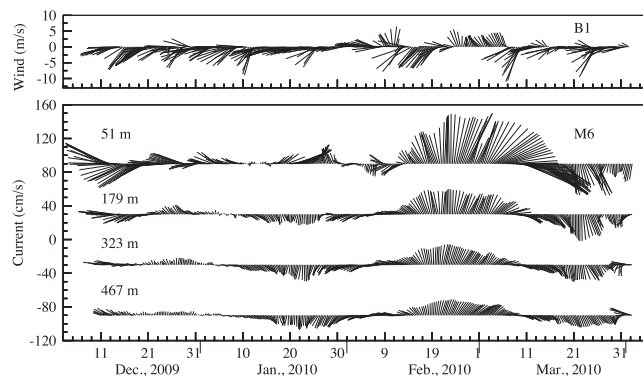


Figure 13. Time series of the 33 h low-pass filtered (top) wind and (bottom) current vectors on buoy B2 (for winds), M6 (for currents) at depths of 51, 179, 323, and 467 m over the time periods from 7 December 2009 to 1 April 2010.

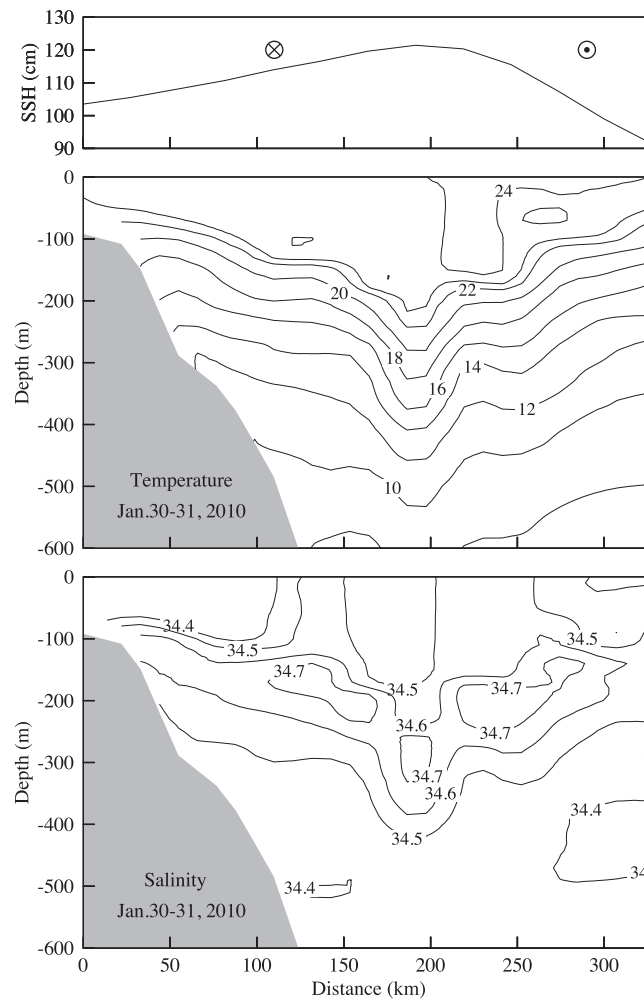


Figure 14. Cross-shelf distributions of sea temperature and salinity on the hydrographic transect S4 taken over the time period of 30–31 January 2010 and corresponding time averaged SSH on the same transect.

the reference velocity in the geostrophic velocity calculation, the calculated geostrophic velocities matched reasonably with observed velocities at these three stations, though they were unable to resolve the observed high-mode vertical shear features (Figure 18, top).

Our analysis suggested that the presence of a significant barotropic velocity component prevents defining the SCSWC based mainly on the geostrophic calculation with the LNM at the bottom. This can be seen more clearly from the momentum balance analysis on transects M1–M3 and M4–M6. With x and y the along-shelf and cross-shelf coordinates, the cross-shelf momentum equation takes on the form

$$fuD = -gD \frac{\partial \zeta}{\partial y} - \frac{g}{\rho_o} \int_{-H}^{\zeta} \frac{\partial}{\partial y} \left(\int_z^{\zeta} \rho dz' \right) dz + \frac{\tau_{sy} - \tau_{by}}{\rho_o} + F_v, \quad (1)$$

where z is the vertical axis, u the x component of horizontal velocity, $D = \zeta + H$ the total water depth, ζ the sea surface elevation, ρ the water density, ρ_o the reference density, g the gravitational acceleration, τ_{sy} and τ_{by} the y components of the sea surface wind stress and bottom stress, respectively, and F_v the combination of the vertical integration terms of horizontal diffusion, local change of the cross-shelf velocity, and nonlinear advection. Ignoring the F_v and bottom stress terms, we could estimate the magnitudes of the other terms: the current measurement for the Coriolis force term, the altimeter-derived sea level anomaly for the surface elevation gradient force term, hydrographic data for the baroclinic pressure gradient force term,

velocity in the geostrophic velocity calculation, the geostrophic velocity matched well with the observed velocity below 60 m, but it underestimated the magnitude of south-westward flow in the upper 55 m layer. Similarly, the geostrophic velocity calculated using the bottom as LNM showed a constant bias of ~ 20 cm/s at M2 and of ~ 15 cm/s at M3 (Figure 17, bottom). When the observed velocity at 60 m was added as the reference velocity in the geostrophic velocity calculation, the calculated geostrophic and observed velocities matched well at M2 and were in reasonable agreement in the upper 220 m layer at M3.

The M4–M6 transect was oriented across the shelf break. The calculated along-isobath geostrophic velocities computed with the LNM set to the bottom at M4 and M5 and 1000 m at M6 showed significant differences of ~ 20 , ~ 3 – 4 , and ~ 10 cm/s compared to the observed velocities at M4, M5, and M6, respectively (Figure 18).

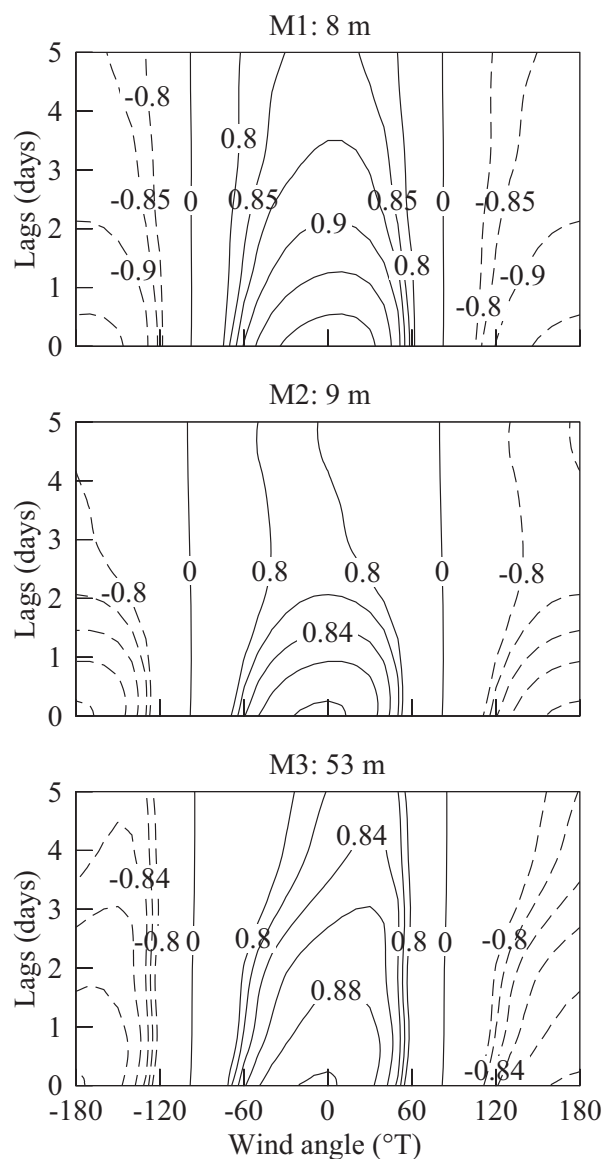


Figure 15. Correlations between the 33 h low-pass filtered southwestward, near-surface subtidal current, and surface wind velocity with angle range of -180° to 180° on M1, M2, and M3. The critical value was 0.29 for a 95% confidence level.

and wind recorded on buoys for the surface wind stress term. The geostrophic flow with a LNM at the bottom was equivalent here to the balance between the Coriolis and baroclinic pressure gradient force terms. On both M1-M3 and M4-M6 transects, we found that the southwestward, along-isobath vertically integrated water transport was mainly balanced by the surface elevation gradient force (Table 3). Thus, to lowest order, the flow would be geostrophic, with a first-order variation driven by the surface wind stress. Such a geostrophic flow would exhibit vertical shear created by the baroclinic pressure gradient. Clearly the observed circulation over the NSCS shelf in winter includes both barotropic and baroclinic components.

It should be pointed out here that in previous studies, there was direct current measurements used to support the existence of SCSWC. However, since most of those direct current measurements were made for short periods (1 week or less), they may have contained short-term current variability due to episodic eddies or intrusion of the buoyancy-driven flow from the slope that prevented clear evidence of the barotropic components.

The moored current measurements captured the movement of an anticyclonic eddy, which originated from the southwest coast of Taiwan and moved southwestward along the slope. Like other eddies reported in previous studies [Yuan *et al.*, 2007; Wang *et al.*, 2008], the movement of this eddy seemed to be trapped over the slope. We agreed with previous studies that its movement was guided by Rossby waves, but it was unclear to us whether or not the eddy moved due to topographic Rossby waves, which were generated locally over the slope [Veronis, 1966; Rhine, 1967, 1969a, 1969b]. To address this question, we estimated the phase speed of the barotropic topographic Rossby wave over the NSCS slope and compared it to the observed motion of the anticyclonic eddy detected in the altimeter SLA images.

The internal Rossby radius of deformation (defined as $R_i = NH/f$, where N is the Brunt-Väisälä frequency, H the local depth, and f the local Coriolis parameter) estimated using the hydrographic survey data taken over the slope in the 2006–2007 and 2009–2010 winters was ~ 50 km (with $N \sim 10^{-3}$) over the NSCS slope. Assuming that the topographic Rossby wavelength was larger than R_i [Rhine, 1970] and the flow was under

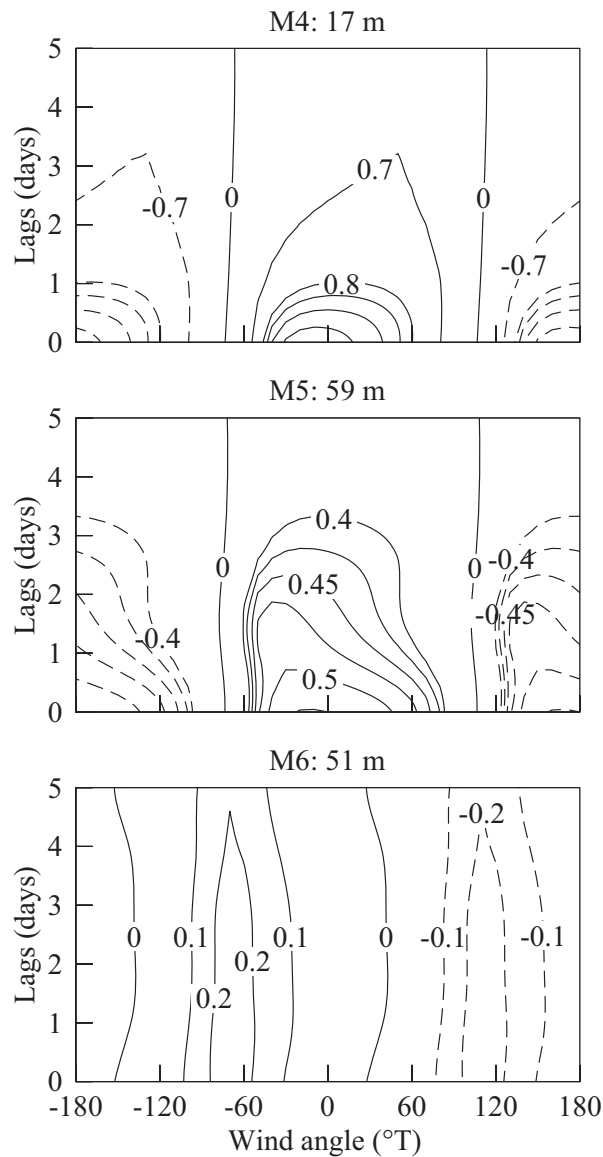


Figure 16. Correlations between the 33 h low-pass filtered southwestward, near-surface subtidal current, and surface wind velocity with angle range of -180° to 180° on M4, M5, and M6. The critical value was 0.21 for a 95% confidence level.

topographic Rossby wave played an equivalent or even dominant role in guiding the southwest movement of the anticyclonic eddy. Considering a wavelength scale of 100 km, the phase speed of the *topographic* Rossby wave $C_p = -\beta_T/k^2$ could be 1.1–5.6 cm/s. Adding the phase speed of the β -plane Rossby wave produced a total phase speed of $O(10 \text{ cm/s})$, which was similar to the observed motion ($\sim 9\text{--}10 \pm 3 \text{ cm/s}$) of the anticyclonic eddy seen in the altimeter SSH images.

6. Conclusions

Eight ADCP moorings were deployed over the NSCS shelf and slope with current measurements made throughout the water column in vertical bin lengths varying from 4 to 16 m during 2006 December through February 2007 and December 2009 through March 2010, respectively. Rotary spectrum analysis showed two peaks at diurnal and semidiurnal tidal periods, with the diurnal tidal energy dominant. The clockwise-rotating tidal energy was much larger than the counterclockwise-rotating tidal energy, suggesting that

quasi-geostrophic condition, the linear vorticity equation with taking the local topography into account can be written as

$$\frac{\partial}{\partial t} \nabla^2 \psi - \left(-\frac{f}{h} \frac{\partial h}{\partial y} + \beta \right) \frac{\partial \psi}{\partial x} = 0, \quad (2)$$

where x and y the along-shelf and cross-shelf coordinates, $h = H - h_B(y)$, H was the constant water depth off the slope, $h_B(y)$ was the topographic height with a positive gradient as y increased, ψ the geostrophic stream function, and $\beta = df/dy$. Defining $\beta_T = -\frac{f}{h} \frac{\partial h}{\partial y} = \frac{f}{h} \frac{\partial h_B}{\partial y}$ and $\psi = Ae^{i(kx+ly-\omega t)}$, the dispersion relation of the Rossby wave with consideration of both topography and β is

$$\omega = -\frac{(\beta_T + \beta)k}{k^2 + l^2}, \quad (3)$$

where k and l are the x and y wave numbers, respectively. On the NSCS slope, f varies from $\sim 22^\circ\text{N}$ at M8 to $\sim 19^\circ\text{N}$ at M6, so that $\beta \sim 2.2 \times 10^{-13} \text{ cm}^{-1} \text{ s}^{-1}$. The topographic slopes around those two areas are $2.0\text{--}8.0 \times 10^{-3}$, so that $\beta_T \sim 4.7 \times 10^{-13}$ to $2.2 \times 10^{-12} \text{ cm}^{-1} \text{ s}^{-1}$ for $h \sim H \sim 2000 \text{ m}$. For an eddy moving southwestward along the slope, β_T was the same order as or even 1 order of magnitude larger than β , suggesting that the

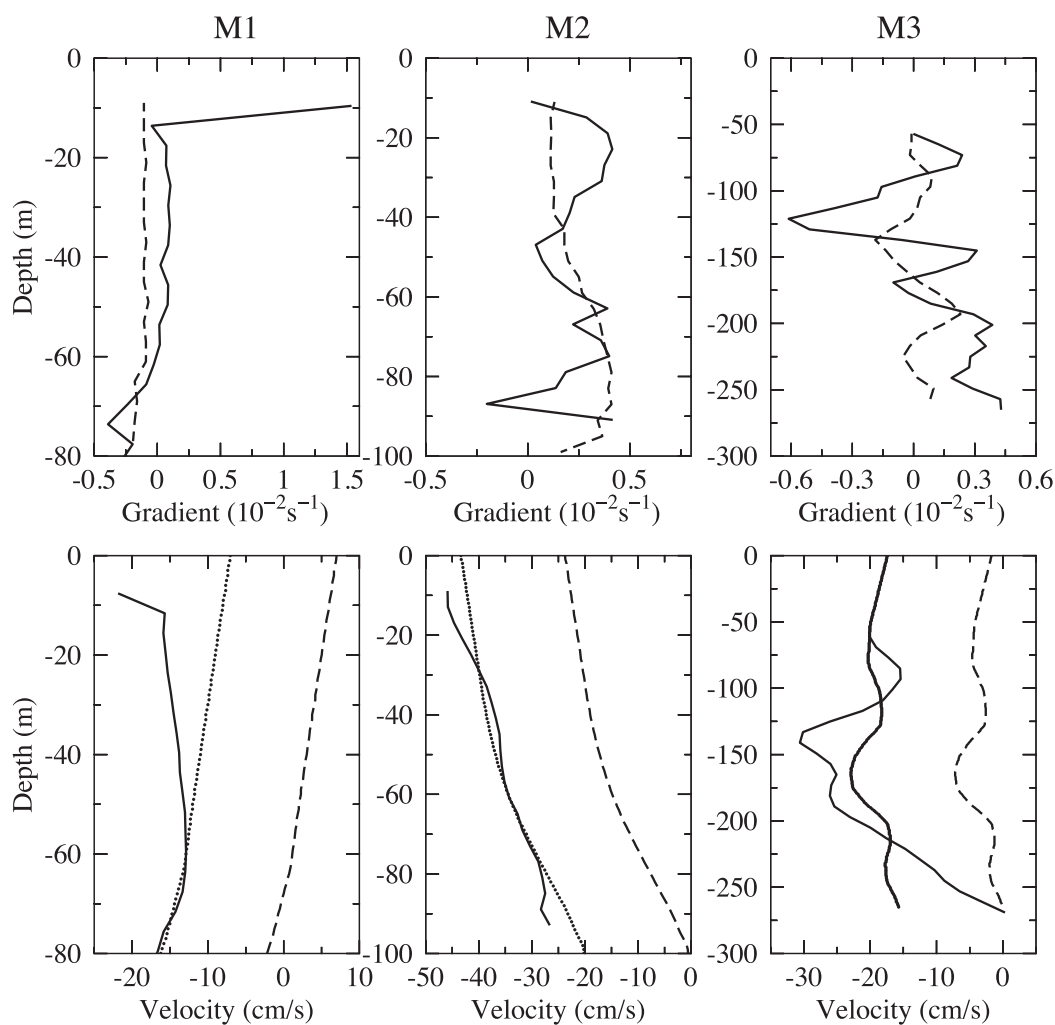


Figure 17. (top) Vertical shears of observed and computed velocities on M1, M2, and M3. Solid line: observed; dashed line: computed using the thermal wind relation. (bottom) Comparison of vertical distributions of observed and computed velocities at M1, M2, and M3. Solid line: observed; dashed line: the geostrophic velocity computed based on the thermal wind relation with a reference of no motion at the bottom; dots: absolute computed geostrophic velocity with the observed velocity at the depth of 60 m as a reference level velocity.

clockwise-rotating tidal currents characterized the NSCS shelf. The vertical structure of the diurnal tidal currents varied significantly in space: a well-defined first-baroclinic mode internal tidal signal with a 180° phase offset at the surface and bottom was observed at one site, while the surface-bottom phase differences were smaller at other measurement sites. The CC-FVCOM was used to examine the physical mechanisms responsible for the spatial variability of the internal diurnal tides, with good agreement found in the vertical structures of the model-predicted and observed diurnal tidal currents at the mooring sites. These model results suggested that the diurnal tidal currents over the NSCS shelf were characterized by the baroclinic Kelvin waves that propagated along isobaths over the slope with a wavelength of about 300 km and a cross-shelf scale of 100–200 km. The vertical structure of these tidal waves was predominantly the first baroclinic mode with reversed direction of tidal currents in the upper and lower layers. The phase difference of the tidal current in the vertical varied in different flow zones, significant around the maximum tidal current magnitude zone and smaller around the transition zone between clockwise and counterclockwise tidal currents.

The wintertime subtidal circulation over the NSCS shelf was mainly southwestward flow driven by the northeasterly surface wind stress with episodic influences of mesoscale eddies. A warm-core anticyclonic eddy with a radius of ~ 100 km originated from the southwestern coast of Taiwan and propagated southwestward along the slope through the moored current meter array in the 2009–2010 winter. The eddy flow was surface-intensified with a swirl speed of >50 cm/s and a vertical scale of 400 m. In the absence of

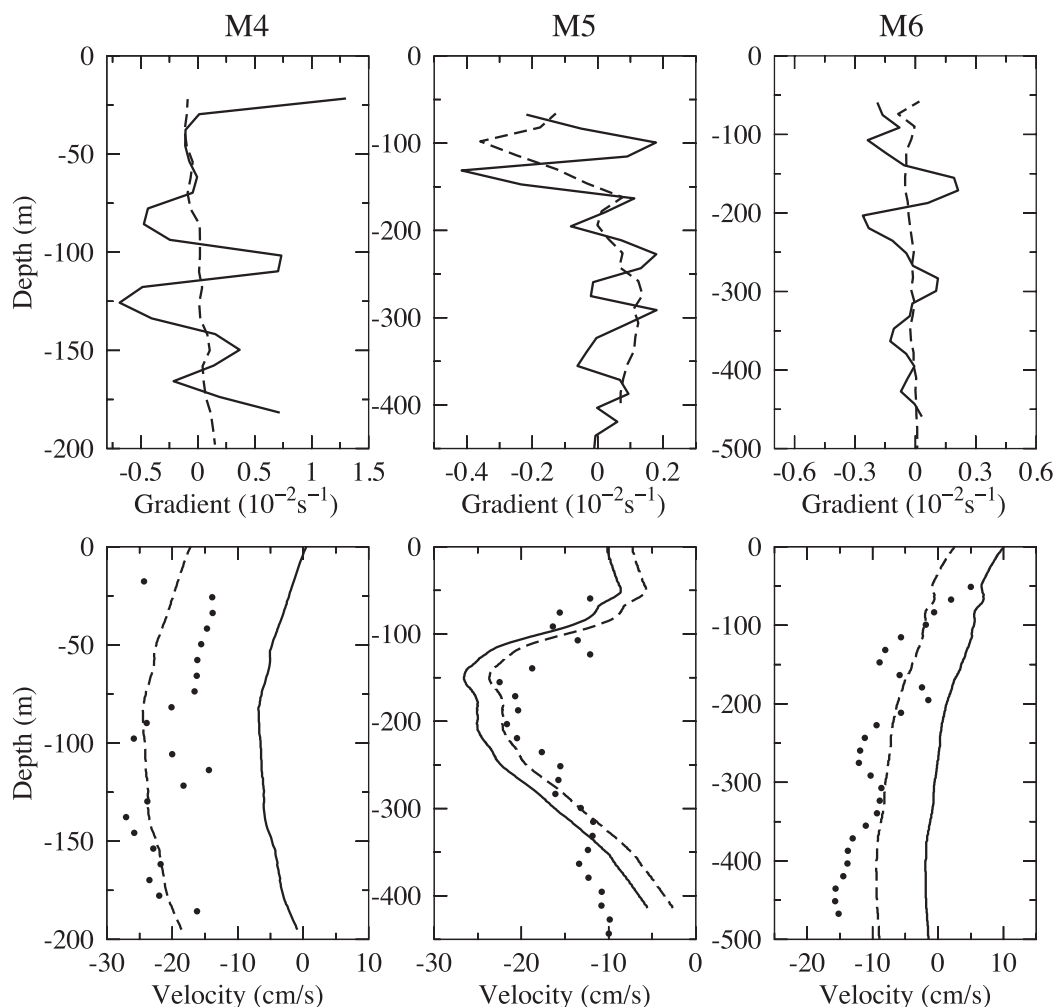


Figure 18. (top) Vertical shears of observed and computed velocities on M4, M5, and M6. Solid line: observed; dashed line: computed using the thermal wind relation. (bottom) Comparison of vertical distributions of observed and computed velocities at M4, M5, and M6. Solid line: observed; dashed line: the geostrophic velocity computed based on the thermal wind relation with a reference of no motion at the bottom or at the 1000 m; dots: absolute computed geostrophic velocity with the observed velocity at the depth of 100 m as a reference level velocity.

eddies and onshore deep slope water intrusion, the observed southwestward flow was highly correlated with the surface wind stress and the maximum correlation occurred with the wind-current angle between -60° and 60° . The bottom-intensified current was observed at the shelf break, with an opposite direction to the surface flow. This flow was less correlated with the surface wind stress and observed anticyclonic eddy, suggesting there was a buoyancy-driven process over the NSCS slope in addition to the wind and eddy. The southwestward movement of the observed anticyclonic eddy seemed to be trapped over the slope, likely guided by a combination of β -plane and topographic Rossby waves.

Table 3. The Momentum Balance Analysis on Transect M1-M3 and M4-M6

Station	Coriolis fuD	Barotropic $-gD \frac{\partial \zeta}{\partial y}$	Baroclinic $-\frac{g}{\rho_0} \int_{-H}^{\zeta} \frac{\partial}{\partial y} \left(\int_{-H}^{\zeta} \rho dz' \right) dz$	Wind Stress $\frac{\tau_{xy}}{\rho_0}$
M1	-6.3×10^{-4}	-8.4×10^{-4}	-2.1×10^{-4}	-2.3×10^{-5}
M2	-1.9×10^{-3}	-1.4×10^{-3}	4.0×10^{-4}	-2.3×10^{-5}
M3	-2.9×10^{-3}	-2.5×10^{-3}	-2.2×10^{-4}	-2.3×10^{-5}
M4	-2.0×10^{-3}	-6.7×10^{-4}	-1.9×10^{-4}	-8.6×10^{-6}
M5	-5.9×10^{-3}	-2.9×10^{-3}	2.7×10^{-4}	-8.6×10^{-6}
M6	-6.2×10^{-3}	-9.0×10^{-3}	-1.6×10^{-3}	-8.6×10^{-6}

Observations did not support the existence of a permanent wintertime South China Sea Warm Current (SCSWC). Comparisons of the observed along-isobath vertical current shears at the moorings with geostrophic current shears computed with different reference levels of no motion and analysis of the vertically integrated cross-isobath momentum balance both indicated that to lowest order, the along-isobath flow would be geostrophic, with first-order variations driven by the surface wind stress. Such a geostrophic flow would exhibit vertical shear created by the baroclinic pressure gradient. Clearly the observed circulation over the NSCS shelf in winter includes both barotropic and baroclinic components.

Acknowledgments

The authors want to thank many individuals in the South China Sea Marine Engineering Survey Center who deployed, maintained, and recovered the moorings. R. Li was supported by the SOA 908 Special Project Foundation of China (908-01-ST07 and 908-01-BC10), the National High Tech Project Foundation (863) of China (2008AA09A401), the Administrator Foundation of South Branch, SOA (0683). C. Chen serves as Chief Scientist for the International Center for Marine Studies, Shanghai Ocean University, and his contribution is supported through the "Shanghai Universities First-class Disciplines Project." C. Chen is also serving as Visiting Professor at the School of Marine Sciences, Sun Yat-Sen University and he would like to credit this research to this university. The development of FVCOM was funded by the US NSF Office of Polar Programs through grants ARC0712903, ARC0732084, ARC0804029, and ARC1203393. The authors also want to acknowledge two reviewers whose input helped improve this manuscript.

References

- Beardsley, R. C., and L. K. Rosenfeld (1983), Introduction to the CODE-1 moored array and large-scale data report, in *CODE-1: Moored Array and Large-Scale Data Report*, edited by L. K. Rosenfeld, *Tech. Rep. WHOI-83-23, CODE Tech. Rep. 21*, p. 1216, Woods Hole Oceanogr. Inst., Woods Hole, Mass.
- Beardsley, R. C., T. F. Duda, J. F. Lynch, J. D. Irish, S. R. Ramp, C.-S. Chiu, T. Y. Tang, Y.-J. Yang, and G. Fang (2004), Barotropic tide in the north-east South China Sea, *IEEE J. Oceanic Eng.*, *29*, 1075–1086.
- Caruso, M., G. G. Gawarkiewicz, and R. Beardsley (2006), Interannual variability of the Kuroshio Current intrusion in the South China Sea, *J. Oceanogr.*, *62*, 559–575.
- Chang, M. H., R. C. Lien, T. Y. Tang, E. A. D'Asaro, and Y. J. Yang (2006), Energy flux of nonlinear internal waves in northern South China Sea, *Geophys. Res. Lett.*, *33*, L03607, doi:10.1029/2005GL025196.
- Chen, C. (2000), A modeling study of episodic cross-frontal water transports over the inner shelf of the South Atlantic Bight, *J. Phys. Oceanogr.*, *30*, 1722–1742.
- Chen, C., and L. Xie (1997), A numerical study of wind-induced, near-inertial oscillations over the Texas-Louisiana shelf, *J. Geophys. Res.*, *102*(C7), 15,583–15,593.
- Chen, C., R. O. Reid, and W. D. Nowlin Jr. (1996), Near-inertial oscillations over the Texas-Louisiana shelf, *J. Geophys. Res.*, *101*(C2), 3509–3524.
- Chen, C., H. Liu, and R. C. Beardsley (2003), An unstructured, finite-volume, three-dimensional, primitive equation ocean model: Application to coastal ocean and estuaries, *J. Atmos. Oceanic Technol.*, *20*, 159–186, doi:10.1175/1520-0426.
- Chen, C., R. C. Beardsley, and G. Cowles (2006a), An unstructured grid, finite-volume coastal ocean model (FVCOM) system, *Oceanography*, *19*, 78–89, doi:10.5670/oceanog.2006.92.
- Chen, C., R. C. Beardsley, and G. Cowles (2006b), An unstructured grid, finite-volume coastal ocean model-FVCOM user manual, 2nd ed., *SMAST/UMASSD Tech. Rep. 06-0602*, 318 p., Univ. of Mass.-Dartmouth, New Bedford, Mass.
- Chen, C., Z. Lai, R. C. Beardsley, Q. Xu, H. Lin, and N. T. Viet (2012), Current separation and upwelling over the southeast shelf of Vietnam in the South China Sea, *J. Geophys. Res.*, *117*, C03033, doi:10.1029/2011JC007150.
- Chen, C., et al. (2013), An unstructured-grid, finite-volume community ocean model FVCOM user manual, 3rd ed., *SMAST/UMASSD Tech. Rep. 13-0701*, p. 404, Univ. of Mass.-Dartmouth, New Bedford, Mass.
- Ding, Y., C. Chen, R. C. Beardsley, X. Bao, M. Shi, Y. Zhang, Z. Lai, R. Li, H. Lin, and N. T. Viet (2013), Observational and model studies of the circulation in the Gulf of Tonkin, South China Sea, *J. Geophys. Res. Oceans*, *118*, 6495–6510, doi:10.1002/2013JC009455.
- Duda, T. F., and L. Rainville (2008), Diurnal and semidiurnal internal tide energy flux at a continental slope in the South China Sea, *J. Geophys. Res.*, *113*, C03025, doi:10.1029/2007JC004418.
- Duda, T. F., J. F. Lynch, J. D. Irish, R. C. Beardsley, S. R. Ramp, C. S. Chiu, T. Y. Tang, and Y.-J. Yang (2004), Internal tide and nonlinear internal wave behavior at the continental slope in the northern South China Sea, *IEEE J. Oceanic Eng.*, *29*, 1105–1130.
- Fang, G., W. D. Fang, Y. Fang, and K. Wang (1998), A survey of studies on the South China Sea upper ocean circulation, *Acta Oceanogr. Taiwan.*, *37*, 1–16.
- Fang, G., Y. Kwok, K. Yu, and Y. Zhu (1999), Numerical simulation of principal tidal constituents in the South China Sea, Gulf of Tonkin and Gulf of Thailand, *Cont. Shelf Res.*, *19*, 845–869.
- Farris, A., and M. Wimbush (1996), Wind-induced Kuroshio intrusion into the South China Sea, *J. Oceanogr.*, *52*, 771–784.
- Guan, B. X. (1978), The warm current in the South China Sea—A current flowing against the wind in winter in the open sea off Guangdong Province [in Chinese with English abstract], *Oceanol. Limnol. Sin.*, *9*, 117–127.
- Guan, B. X., and S. J. Chen (1964), The current systems in the near sea area of China Seas [in Chinese], report, pp. 1–85, Natl. Mar. Surv., Beijing.
- Guo, P., W. Fang, Z. Gan, R. Chen, and X. Long (2006), Internal tide characteristics over northern South China Sea continental slope, *Chin. Sci. Bull.*, *50*(24), 17–25.
- Guo, P., W. Fang, C. Liu, and F. Qiu (2012), Seasonal characteristics of internal tides on the continental shelf in the northern South China Sea, *J. Geophys. Res.*, *117*, C04023, doi:10.1029/2011JC007215.
- Guo, Z. X., T. H. Yang, and D. Z. Qiu (1985), The South China Sea Warm Current and the SW-ward current on its right side in winter [in Chinese with English abstract], *Trop. Oceanol.*, *4*(1), 1–9.
- Hsueh, Y., and L. Zhong (2004), A pressure-driven South China Sea Warm Current, *J. Geophys. Res.*, *109*, C09014, doi:10.1029/2004JC002374.
- Jan, S., C. S. Chern, J. Wang, and S.-Y. Chao (2007), Generation of diurnal K1 internal tide in the Luzon Strait and its influence on surface tide in the South China Sea, *J. Geophys. Res.*, *112*, C06019, doi:10.1029/2006JC004003.
- Kelvin, L. (1879), On gravitational oscillations of rotating water, *Proc. R. Soc. Edinburgh*, *10*, 92–100.
- Klymak, J. M., M. H. Alford, R. Pinkel, R. C. Lien, and Y. J. Yang (2011), The breaking and scattering of the internal tide on a continental slope, *J. Phys. Oceanogr.*, *41*, 926–945.
- Kourafalou, V. H., L. Y. Oey, J. D. Wang, and T. N. Lee (1996), The fate of river discharge on the continental shelf: 1. Modeling the river plume and the inner shelf coastal current, *J. Geophys. Res.*, *101*(C2), 3415–3434.
- Li, L., W. D. Nowlin Jr., and J. L. Su (1998), Anticyclonic rings from the Kuroshio in the South China Sea, *Deep Sea Res., Part 1*, *45*, 1469–1482.
- Liang, X., X. Zhang, and J. Tian (2005), Observation of internal tides and near-inertial motions in the upper 450 m layer of the northern South China Sea, *Chin. Sci. Bull.*, *50*(24), 2890–2895.
- Lien, R. C., T. Y. Tang, M. H. Chang, and E. A. D'Asaro (2005), Energy of nonlinear internal waves in the South China Sea, *Geophys. Res. Lett.*, *32*, L05615, doi:10.1029/2004GL022012.

- Liu, C., W. Zhuang, H. Xia, and Y. Du (2012), Mesoscale observation in the northeast South China Sea during winter 2009–2010, *Acta Oceanol. Sin.*, *1*, 8–16.
- Matsuno, T., J. S. Lee, and S. Yano (2009), The Kuroshio exchange with the South China and East China Sea, *Ocean Sci.*, *5*, 303–312.
- Mellor, G. L., and T. Yamada (1982), Development of a turbulence closure model for geophysical fluid problem, *Rev. Geophys.*, *20*(4), 851–875, doi:10.1029/RG020i004p00851.
- Metzger, E. J., and H. E. Hurlburt (2001), The nondeterministic nature of Kuroshio penetration and eddy shedding in the South China Sea, *J. Phys. Oceanogr.*, *31*, 1712–1732.
- Pawlowicz, R., R. Beardsley, and S. Lentz (2002), Classical tidal harmonic analysis including error estimates in MATLAB using T_TIDE, *Comput. Geosci.*, *28*, 929–937, doi:10.1016/S0098-3004(02)00013-4.
- Rhine, P. B. (1967), The influence of bottom topography on long-period waves in the ocean, PhD thesis, Univ. of Cambridge, Cambridge, U. K.
- Rhine, P. B. (1969a), Slow oscillations in an ocean of varying depth. Part I. Abrupt topography, *J. Fluid Mech.*, *37*, 161–189.
- Rhine, P. B. (1969b), Slow oscillations in an ocean of varying depth. Part 2. Islands and seamounts, *J. Fluid Mech.*, *37*, 191–205.
- Rhine, P. B. (1970), Edge-, bottom- and Rossby waves in a rotating stratified fluid, *Geophys. Fluid Dyn.*, *1*, 273–302.
- Shaw, P. T. (1991), The seasonal variation of the intrusion of the Philippine Sea water into the South China Sea, *J. Geophys. Res.*, *96*(C1), 821–827.
- Smagorinsky, J. (1963), General circulation experiments with the primitive equations, I. The basic experiment, *Mon. Weather Rev.*, *91*, 99–164, doi:10.1175/15200493.
- Su, J. (2004), Overview of the South China Sea circulation and its influence on the coastal physical oceanography outside the Pearl River Estuary, *Cont. Shelf Res.*, *24*, 1745–1760.
- Su, J., B. X. Guan, and J. Z. Jiang (1990), The Kuroshio, Part I. Physical features, *Oceanogr. Mar. Biol. Annu. Rev.*, *28*, 11–71.
- Tai, J. H., T. Y. Tang, and G. Gawarkiewicz (2010), Instability of the Kuroshio in Luzon Strait: Effects of ridge topography and stratification, *J. Oceanogr.*, *66*(4), 523–538.
- Veronis, G. (1966), Rossby waves with bottom topography, *J. Mar. Res.*, *24*, 338–349.
- Wang, G., J. Su, and P. C. Chu (2003), Mesoscale eddies in the South China Sea observed with altimeter data, *Geophys. Res. Lett.*, *30*(21), 2121, doi:10.1029/2003GL018532.
- Wang, D., H. Xu, J. Lin, and J. Hu (2008), Anticyclonic eddies in the Northeastern South China Sea during winter 2003/2004, *J. Oceanogr.*, *54*, 925–935.
- White, W. B. (2000), Tropic coupled Rossby waves in the Pacific ocean-atmosphere system, *J. Phys. Oceanogr.*, *30*(6), 1245–1264.
- Wyrtki, K. (1961), Physical oceanography of the Southeast Asian water, in *NAGA Report: Scientific Result of Marine Investigation of the South China Sea and Gulf of Thailand 1959–1961*, vol. 2, pp. 155–160, Scripps Inst. of Oceanogr., La Jolla, Calif.
- Xu, X., Z. Qui, and H. Chen (1982), Summary of the horizontal circulation in the South China Sea [in Chinese with English abstract], in *Chinese Society of Oceanology and Limnology Proceedings of the Hydrology and Meteorology*, pp. 137–145, Science, Beijing.
- Xu, Z., B. Yin, Y. Hou, and Y. Xu (2013), Variability of internal tides and near-inertial waves on the continental slope of the northwestern South China Sea, *J. Geophys. Res.*, *118*, 197–211, doi:10.1029/2012JC008212.
- Xue, H., F. Chai, N. Pettigrew, D. Xu, M. Shi, and J. Xu (2004), Kuroshio intrusion and the circulation in the South China Sea, *J. Geophys. Res.*, *109*, C02017, doi:10.1029/2002JC001724.
- Yang, J., D. Wu, and X. Lin (2008), On the dynamics of the South China Sea Warm Current, *J. Geophys. Res.*, *113*, C08003, doi:10.1029/2007JC004427.
- Yuan, D., W. Han, and D. Hu (2007), Anti-cyclonic eddies northwest of Luzon in summer–fall observed by satellite altimeters, *Geophys. Res. Lett.*, *34*, L13610, doi:10.1029/2007GL029401.
- Zhao, Z., V. Klemas, Q. Zheng, and X.-H. Yan (2004), Remote sensing evidence for baroclinic tide origin of internal solitary waves in the northeastern South China Sea, *Geophys. Res. Lett.*, *31*, L06302, doi:10.1029/2003GL019077.
- Zu, T., J. Gan, and S. Erofeeva (2008), Numerical study of tide and tidal dynamics in the South China Sea, *Deep Sea Res., Part I*, *55*, 137–154, doi:10.1016/j.dsr.2007.10.007.